Contributions to Mineralogy and Petrology (2024) 179:45
https://doi.org/10.1007/s00410-024-02118-z

ORIGINAL PAPER

Trace element partitioning in the lunar magma ocean: an experimental study

Cordula P. Haupt[1] · Christian J. Renggli[1,2] · Arno Rohrbach[1] · Jasper Berndt[1] · Sabrina Schwinger[3] · Maxime Maurice[4,5] · Maximilian Schulze[6] · Doris Breuer[3] · Stephan Klemme[1]

Received: 9 October 2023 / Accepted: 10 March 2024

Abstract

Modeling the behavior of trace elements during lunar magma ocean solidification is important to further our understanding of the chemical evolution of the Moon. Lunar magma ocean evolution models rely on consistent datasets on how trace elements partition between a lunar silicate melt and coexisting minerals at different pressures, temperatures, and redox conditions. Here we report new experimental trace element partition coefficients (D) between clinopyroxene (cpx), pigeonite, orthopyroxene, plagioclase, olivine (ol), and silicate melt at conditions relevant for the lunar magma ocean. The data include $D^{cpx-melt}$ at ambient and high pressures (1.5 GPa and 1310 °C), and partition coefficients at ambient pressure for pig, opx, ol, and pl. Overall, clinopyroxene is a phase that may control the fractionation of key geochemical trace element ratios, such as Lu/Hf and Sm/Nd, during the evolution of the lunar magma ocean. We explore the impact of the new silicate $D^{mineral-melt}$ on the trace element evolution of the lunar magma ocean and we find that accessory phosphate minerals, such as apatite or whitlockite are of critical importance to explain the observed trace element and isotopic signature of the KREEP reservoir on the Moon. The new partition coefficients were applied to calculate the trace element evolution of the residual melts of the crystallizing lunar magma ocean and we propose a new trace element composition for the urKREEP reservoir. The new data will be useful for future thermo-chemical models in order to adequately predict the duration of the lunar magma ocean and the age of the Moon.

Keywords Experimental petrology · Geochemistry · partition coefficient · LAICPMS · Lunar magma ocean · Oxygen fugacity · Moon · High pressure experiment · Trace element partitioning · urKREEP

Introduction

It is widely accepted that a collision of a Mars-sized planetary body with the Earth led to the formation of the Moon (e.g., Canup and Righter 2000), and that the release of kinetic energy of the collision resulted in the formation of large and deep magma oceans on the Moon and the Earth (e.g., Elkins-Tanton et al. 2011). Several recent experimental studies and geodynamic models show how the lunar magma ocean (LMO) differentiated into a layered cumulate mantle (Elkins-Tanton et al. 2011; Elardo et al. 2011; Lin et al. 2017; Charlier et al. 2018; Rapp and Draper 2018; Johnson et al. 2021; Schmidt and Kraettli 2022).

Moreover, thermophysical modeling (Maurice et al. 2020) aimed to determine the duration of the lunar magma ocean stage by combining a computed solidification sequence with thermal evolution of the LMO and the lunar mantle, and additionally trace element evolution. The outcomes of

Communicated by Othmar Müntener.

✉ Cordula P. Haupt
chaupt1@uni-muenster.de

[1] Institut für Mineralogie, Universität Münster, Corrensstr. 24, 48149 Münster, Germany

[2] Max-Planck-Institut für Sonnensystemforschung, Justus-Von-Liebig-Weg 3, 37077 Göttingen, Germany

[3] Institut für Planetenforschung, Deutsches Zentrum für Luft- und Raumfahrt (DLR), Rutherfordstr. 2, 12489 Berlin, Germany

[4] Department of Earth, Environmental and Planetary Sciences, Rice University, Houston, USA

[5] Laboratoire de Météorologie Dynamique, IPSL, CNRS, 4 Place Jussieu, 75252 Paris, France

[6] Institut für Geologie und Mineralogie, Universität zu Köln, Zülpicher Str. 49b, 50674 Köln, Germany

Published online: 13 April 2024

the combined thermal and chemical fractionation modeling allowed to calculate the isotopic evolution of ^{176}Lu–^{177}Hf and ^{147}Sm–^{143}Nd systems, which were used to integrate isotopic compositions and absolute ages of lunar rocks (Ferroan Anorthosite sample FAN 60025 and Kalahari 009, Borg et al. 2011, Snape et al. 2018) and to calculate the timing of LMO crystallization and the age of the Moon (Maurice et al. 2020). Their preferred model predicts that the solidification of the LMO took ~ 170 Ma. This model depends critically on the depth of the initial LMO and trace element partition coefficients of Lu, Hf, Sm, and Nd between the LMO residuum and crystallizing mineral phases.

Maurice et al. (2020) used partition coefficients originally intended for terrestrial conditions (e.g., McDade et al. 2003; Klemme et al. 2006) and they showed that trace element partition coefficients ($D^{mineral-melt}$) control the trace element evolution of the LMO and hence lunar age predictions (Maurice et al. 2020 and Fig. 4 therein). From these authors' work it can be concluded that it is clinopyroxene that exerts a primary control over the evolution of nearly all trace elements.

Numerous studies determined $D^{cpx-melt}$ at conditions relevant to Earth (e.g., Hauri et al. 1994; McDade et al. 2003; Hill et al. 2011) and several attempts have been made to parameterize $D^{cpx-melt}$ as a function of pressure (P), temperature (T), and chemical composition of the clinopyroxene (Wood and Blundy 1997; Hill et al. 2011; Sun and Liang 2012; Dygert et al. 2014—whenever cited in this paper, the corrigendum of Dygert et al. 2015 is included). Most studies agree that $D^{cpx-melt}$ is mainly controlled by temperature and the pyroxene composition (e.g., Hill et al. 2000, 2011; Olin and Wolff 2010). However, crystallization of melts on the Moon occurs at an oxygen fugacity (fO_2), much more reducing compared to the Earth's mantle, which may limit the validity of the aforementioned predictive models without verification.

The lunar mantle is significantly more reduced (given relative to the iron–wüstite buffer ΔIW–1, Sato 1976; Wadhwa 2008) than the current terrestrial mantle (~ ΔIW + 3, Mallmann and O'Neill 2009), so that Fe on the Moon occurs mainly as Fe^{2+}, and consequently, ferric iron (Fe^{3+}) is almost absent in lunar pyroxenes and melts (Herzenberg and Riley 1970; Muir et al. 1970; Sato 1976). Moreover, Ti and Cr occur in different valence states (Ti^{4+} and Ti^{3+}, Cr^{3+} and Cr^{2+}; Papike et al. 1991). Additionally, the bulk silicate Moon (BSM) is significantly depleted in moderately (e.g., Na, K) to highly volatile elements (e.g., H, C) compared to the bulk silicate Earth (BSE; O'Neill 1991) and contains more Fe (9.4–10.9 wt% for BSM compared to ~ 8 wt% for BSE, Schwinger and Breuer 2022; McDonough and Sun 1995) and TiO_2 (0.3 wt% BSM compared to 0.002 wt% BSE, Taylor 1982; McDonough and Sun 1995).

Only a few recent studies report $D^{mineral-melt}$ for minerals that are relevant for the evolution of trace elements in lunar melts, and that were generated experimentally at conditions relevant for the Moon (Dygert et al. 2013, 2014, 2020; Sun and Liang 2013; Snape et al. 2022). Furthermore, these studies report only $D^{mineral-melt}$ for selected trace elements (e.g., Snape et al. 2022: Rb, Sr, Sm, Nd, Lu, Hf, Pb, Th). The most recent study reporting plagioclase and pigeonite $D^{mineral-melt}$ only covers a limited range of temperatures and redox conditions (e.g., Dygert et al. 2020: fO_2: IW, FMQ, T: < 1150 °C) whereas the T range for LMO crystallization spans between ~ 1800–1000 °C (e.g., Schmidt and Kraettli 2022). Data for clinopyroxene grown at conditions relevant for the Moon cover a wide range of trace elements (Dygert et al. 2014), but Mg numbers (Mg#, molar Mg/(Mg + Fe)) of clinopyroxene are low (Mg# = 4.5–52) and are only applicable to a very restricted episode in lunar evolution when Fe and Ti-rich phases started to crystallize (< 90% solidification, Snyder et al. 1992, Supplementary Material Fig. S1).

In summary, there is currently no complete dataset of partition coefficients for major mantle minerals such as clinopyroxene (cpx), pigeonite (pig), plagioclase (pl), and olivine (ol) at conditions relevant for the Moon. In order to address these issues, we performed experiments to determine new trace element partition coefficients ($D^{mineral-melt}$) for clinopyroxene, low-Ca pyroxenes (orthopyroxene and pigeonite), olivine, and plagioclase with melt compositions and mineral compositions relevant for the Moon at pressures of 1 atm to 1.5 GPa (clinopyroxene only) and at temperatures between 1200–1310 °C. The new $D^{mineral-melt}$ enable a more realistic assessment of trace element fractionation during the evolution of the LMO and prediction of the urKREEP trace element composition.

Experimental and analytical methods

Starting materials

The starting material compositions were chosen based on an experimental study of Rapp and Draper (2018), who simulated the fractionation of the LMO from a BSM composition corresponding to the Lunar Primitive Upper Mantle (LPUM: Longhi 2003, 2006). To determine clinopyroxene-melt partition coefficients, we designed a starting material based on clinopyroxene and melt compositions of Rapp and Draper's run (L-PC16), where clinopyroxene is in equilibrium with a silicate melt. Our starting material was created by using the aforementioned experiment, adding clinopyroxene and melt in a volumetric ratio of 2/3. Clinopyroxene saturation was ensured by adding extra CaO (i.e., 4 wt% of CaO for starting mix CHV-6B and 6 wt% for CHV-6C). Additionally, starting material CHV-10 represents the major element clinopyroxene composition (L-PC16) reported in Rapp and Draper (2018). To determine $D^{mineral-melt}$ between olivine,

low-Ca pyroxene (pigeonite and orthopyroxene), and melt, the pigeonite and melt compositions from experiment CHV-E281 (starting material CHV-10) were used and starting material CHV-PiM was prepared, using a volumetric pig/melt of 1/2.

All starting materials were synthesized by mixing high-purity reagent grade oxides and carbonates (SiO_2, Al_2O_3, TiO_2, MgO, Cr_2O_3, $CaCO_3$, $MnCO_3$, K_2CO_3, Na_2CO_3). To remove any unwanted hydroxide or carbonate, the MgO was fired at 1000 °C for 4 h and the fired powder was subsequently stored in a drying oven at 110 °C. The mixtures were homogenized under ethanol in agate mortars for 40 min and dried under an UV lamp, placed in a Pt-crucible and decarbonated in a box furnace at 1000 °C for 10 h, followed by another 40 min of grinding and mixing. Iron was added to the decarbonated mixture as hematite (Fe_2O_3). Trace elements (Li, Sc, V, Co, Ni, Cu, Zn, As, Rb, Sr, Y, Zr, Nb, Mo, Cs, Ba, La, Ce, Pr, Nd, Sm, Eu, Gd, Tb, Dy, Ho, Er, Tm, Yb, Lu, Hf, Ta, Pb, Th, U) were added as standard solutions with concentrations of 1000 and 10,000 µg/g diluted in 5% HNO_3. The total trace element content in each starting composition (< 3000 µg/g) is within the Henry's Law region (Prowatke and Klemme 2006b). The resulting Fe-bearing mixture was fused in a Pt-crucible at 1400 °C and reground and remixed. A small aliquot of each material (ca. 15 mg) was mounted on a Re-wire loop and fused in a vertical gas-mixing furnace at an fO_2 corresponding to IW at 1400 °C. The resulting glass beads were embedded in epoxy resin, polished and carbon coated for electronprobe microanalysis (EPMA). The remaining starting material powders were stored in a desiccator. The chemical compositions of all starting materials are given in Table 1.

1-atm gas-mixing furnace experiments

Experiments at atmospheric pressure (1-atm) were performed in gas-mixing furnaces (Gero GmbH, Germany) in the experimental petrology laboratories at Universität Münster. We used the wire-loop technique (Donaldson et al. 1975) and 0.2 mm thin Re-wires, because commonly used Pt-wire alloys with Fe at reducing conditions (Grove 1982). To mount the starting material onto the wires, about 30 mg starting material powder was mixed with polyethylene glycol and water. With the help of a homemade cylindrical Teflon mold, the powder slurry was pressed into pellets that contained the metal wire loop. The loops were attached to a Pt-chandelier, which was slowly inserted into the cold zone at the top of the furnace, at T of ~ 200 °C below the liquidus. The CO-CO_2 gas mixtures were then set to the required run conditions and after about 20 min the samples were carefully lowered into the hot zone of the furnace, ensuring that the appropriate gas-mixture was already flowing at a steady state through the furnace. The furnaces were programmed to reach a temperature of 50–100 °C above the liquidus (T_{max}, Table 2, cf., Rapp and Draper 2018) and samples were held there for 1 h. A ramp of 2 °C/h was chosen for the 1-atm experiments, cooling the runs to the final run temperature (Table 2). This temperature (T_{final}) was maintained for at least 40 h after which samples were quenched in air. Details of the individual runs are given in Table 2. Oxygen fugacity (IW to ΔIW–2) in the runs was induced using CO–CO_2 gas mixtures and controlled by Tylan gas mass flow controllers.

High-pressure experiments in the piston cylinder apparatus

In order to assess the effect of pressure and to collect data for volatile elements, we conducted two experiments on CH-V-6C at 1.5 GPa, a pressure within the range of clinopyroxene crystallization predicted by LMO evolution models (e.g., Jing et al. 2022; Rapp and Draper 2018). The experiments at 1.5 GPa (GPC866, YPC568) were run in an end-loaded piston-cylinder apparatus (Boyd and England 1960). The starting materials were placed into graphite lined Pt-capsules and the latter were welded shut after having spent at least 24 h in a drying oven at 110 °C. The graphite sleeves buffer the oxygen fugacity around 1.5 log units above the IW buffer at the chosen run conditions (Medard et al. 2008). The capsules were inserted into ½ inch piston-cylinder assemblies consisting of two inner cylinders made of 6 mm O.D. crushable alumina. The inner parts of the assembly are surrounded by a graphite furnace (Schunk GmbH, Germany), an outer

Table 1 Starting material compositions (wt.%) determined by EPMA, uncertainties given as 1σ standard deviation in brackets

Starting material	Na_2O	MgO	Al_2O_3	SiO_2	K_2O	CaO	FeO	TiO_2	Cr_2O_3	MnO	NiO	Total
CH-V-6C (30)[a]	0.71(2)	10.15(5)	8.66(8)	42.73(11)	0.20(1)	19.21(12)	13.13(6)	1.93(8)	0.12(2)	0.24(1)	0.08(1)	97.17
CH-V-6B (30)	0.74(2)	10.22(5)	11.87(7)	42.15(12)	0.11(1)	17.22(10)	6.77(7)	7.46(32)	0.16(1)	0.22(1)	0.09(1)	97.00
CH-V-10 (20)	< DL	14.01(10)	7.79(1)	50.08(20)	< DL	13.67(15)	11.25(18)	0.55(1)	0.34(3)	0.35(2)	0.08	98.02
PiM[b]	0.83	14.41	8.3	51.49	0.23	10.18	11.77	0.66	0.4	0.32	< DL	98.6

[a]Numbers in brackets correspond to number of analyses per glass

[b]PiM given as nominal composition

< DL for analysis below the detection limit

Table 2 Experimental run conditions and phase proportions

Run	ID	Starting material	P (GPa)	T_{max} (°C)	T_{final} (°C)	Run duration (h)	ΔIW	Phases and modes (%)	ΔFe (%)	$\sum r^2$
120	CHV-E424	CHV-6C	0.0001	1320	1240	48	IW	cpx(11), melt(89)	1.5	1.4
84	CHV-E346	CHV-6C	0.0001	1350	1200	48	−1	cpx(31), melt(67)	2	0.4
84	CHV-E349	CHV-6C	0.0001	1350	1200	48	−1	cpx(29), melt(69)	1.8	0.4
119	CHV-E421	CHV-PiM	0.0001	1320	1270	48	IW	ol(7), opx(5), melt(88)	1.1	1.3
42	CHV-E154- 157[a]	CHV-6C	0.0001	1350	1200	40	−1	cpx(35), melt(65)	1.8	0.8
61	CHV-E281	CHV-10	0.0001	1350	1200	56	−1	cpx(16), pig(10), ol(2), melt(72)	0	0.4
61	CHV-E282	CHV-10	0.0001	1350	1200	56	−1	cpx(17.1), pig(8.9), ol(1.6), melt(72.5)	0	0.8
	GPC866	CHV-6C	1.5	1310	1310	72	+1.5	cpx(29), melt(71)	7.2	0.8
	YPC586	CHV-6C	1.5	1310	1310	72	+1.5	cpx(46), melt(54)	4.9	0.5
54	CHV-E227	CHV-6B	0.0001	1350	1200	48	−2	cpx(24), pl(6), melt(70)	0	0.3
63	CHV-E284	CHV-6B	0.0001	1350	1200	55	−1	cpx(24), pl(6), melt(70)	0	0.6

Pressure given in GPa, T in °C, duration in h, fO_2 given relative to the iron-wüstite buffer (IW) as ΔIW. All experiments conducted at P = 0.0001 GPa were cooled from T_{max} to T_{final} with 2 °C/h. Mineral and melt fractions given in %, as estimated with a linear least squares approach using phase compositions given in wt.% element oxides, accumulated squared residuals of this mass balance given as $\sum r^2$. Fe-loss reported in modal % FeO as calculated in the mass balance calculation

Phase abbreviations are: clinopyroxene = cpx, orthopyroxene = opx, plagioclase = pl, pigeonite = pig, olivine = ol, melt = quenched melt

[a]Experiments CHV-E154, 155, 156, and 157 all conducted in the same run with same phase proportions

Duran glass cylinder (Schott, GmbH, Germany) and a talk sleeve. Calibration of the assembly has been performed using the quartz–coesite transition (Bose and Ganguly 1995) and the $MgCr_2O_4 + SiO_2 = MgSiO_3 + Cr_2O_3$ reaction (Klemme and O'Neill 1997), which results in a friction correction of –13%. Based on our pressure calibration, quoted pressures are accurate within 0.07 GPa. Experimental run temperatures were monitored and controlled using a W–Re-thermocouple (Type D) in conjunction with an Eurotherm controller (Schneider Electric, Germany). Experiments were quenched by shutting off the electric power. The experimental run conditions and phases present in the runs are given in Table 2.

All run products of the 1-atm experiments and Pt-capsules from the high-pressure (high-P) runs were mounted in epoxy-resin and polished with a series of diamond pastes. The mounts were carbon-coated, examined with a scanning electron microscope, and minerals and quenched melts were analyzed quantitatively with EPMA (Fig. 1; Table 2).

Electronprobe microanalysis (EPMA)

Major and minor element compositions of minerals and quenched melts of the run products were analyzed using a JEOL JXA 8530 F Hyperprobe in wavelength-dispersive mode (WDS). Measurements on olivine, pyroxene, and silicate glasses were performed using an acceleration voltage of 15 kV and a beam current of 15 nA. Plagioclase analyses were performed with a beam current of 10 nA. Glasses were analyzed with a defocused electron beam of 10–20 µm diameter, whereas silicate minerals were measured with a beam diameter of 3–5 µm. Further details of the analytical protocol are given by Haupt et al. (2023). The matrix corrections were done using the φ(ρz) procedure (Armstrong 1991).

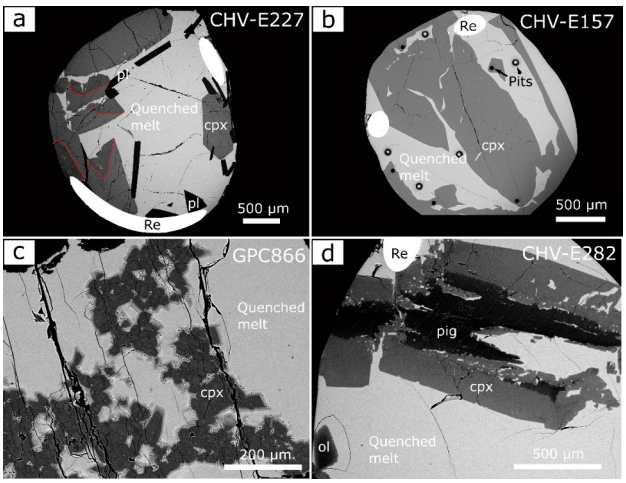

Fig. 1 Back-scattered electron (BSE) images of experimental run products. **a** Idiomorphic clinopyroxene (cpx) with sector zoning (sectors outlined by red dotted lines) and large homogenous plagioclase crystals (pl), **b** large, anhedral, homogeneous clinopyroxene crystals and circular laser ablation pits, **c** high-P experiment with clinopyroxene-aggregates containing slight quench overgrowth and quenched melt, **d** clinopyroxene-pigeonite (pig) intergrowth and olivine (ol). 1-atm runs were performed using Re-wire loops (Re in **a**, **b**, **d**). Note that all experiments contain large homogeneous quenched melt areas

Laser-ablation inductively-coupled plasma mass spectrometry (LA-ICP-MS)

Analysis of trace elements

Trace element concentrations of minerals and quenched melts were analyzed in low resolution mode with laser-ablation inductively-coupled plasma mass spectrometry (LA-ICP-MS) using a pulsed 193 nm ArF excimer laser (Analyte G2, Photon Machines) coupled to an ElementXR mass spectrometer in several sessions. For trace element analysis an ablation rate of 10 Hz was used, measuring 18 s on the background and 40 s on the peak with a washout time of 20 s. Glasses were ablated using a spot size of 65 µm and a spot size of 40 µm for silicate minerals. The following isotopes were analyzed: ^{7}Li, ^{29}Si, ^{43}Ca, ^{45}Sc, ^{47}Ti, ^{49}Ti, ^{51} V, ^{53}Cr, ^{55}Mn, ^{59}Co, ^{60}Ni, ^{65}Cu, ^{66}Zn, ^{75}As, ^{85}Rb, ^{88}Sr, ^{89}Y, ^{90}Zr, ^{93}Nb, ^{95}Mo, ^{115}In, ^{133}Cs, ^{137}Ba, ^{139}La, ^{140}Ce, ^{141}Pr, ^{146}Nd, ^{147}Sm, ^{153}Eu, ^{157}Gd, ^{159} Tb, ^{163}Dy, ^{165}Ho, ^{166}Er, ^{169}Tm, ^{172}Yb, ^{175}Lu, ^{178}Hf, ^{181}Ta, ^{208}Pb, ^{232}Th, ^{238}U. The well-characterized NISTSRM612 glass was utilized for standardization. Calcium was used as an internal standard element for high-Ca pyroxene and plagioclase, Si for low-Ca pyroxene and olivine. Absolute element concentrations had been determined by EPMA beforehand (Supplementary Table S1). Trace element concentrations in the silicate glasses were determined using Ca as internal standard and double checked with Si, showing insignificant variations. As such, only the trace element concentrations of silicate glasses using Ca as internal standard element are reported in Supplementary Table S2. USGS reference materials BIR-1G, BHVO-2G, and BCR-1G were measured as unknowns (secondary reference materials) every ~ 20 LA-ICP-MS spots to assess the analytical accuracy and precision of the measured trace element concentrations (reference concentrations and deviation of the measurements are given in Supplementary Table S4). The compositions of the standard and reference materials were attained from the GeoREM database (preferred values, Jochum et al. 2011).

Two isotopes of Ti were analyzed in almost all sessions (^{47}Ti, ^{49}Ti Supplementary Tables S2, 3), because ^{47}Ti is potentially affected by an isobaric interference with double-charged ^{94}Zr. However, the calculated Ti concentrations using both isotopes are identical within reported uncertainties, given D_{Ti} are determined using concentrations based on ^{47}Ti (Table 3).

Table 3 Major element compositions of minerals and melts analyzed using EPMA given in wt.% element oxides

Run ID	Phase	n	SiO_2	Na_2O	TiO_2	K_2O	CaO	MgO	Al_2O_3	FeO	MnO	Cr_2O_3	NiO	Total
CHV-E424	cpx	15	52.7(6)[a]		0.6(1)	0.003(4)	23.1(2)	16.7(3)	2.4(6)	4.01(7)	0.09(1)	0.6(1)	0.02(2)	100.2
	glass	10	43.8(2)		1.92(6)	0.006(9)	20.5(2)	10.3(1)	10.2(1)	13.5(1)	0.26(4)	0.10(3)		100.6
CHV-E346	cpx	5	51.1(5)		1.1(2)	0.004(4)	23.3(2)	15.7(2)	4.1(3)	4.2(2)	0.10(1)	0.5(1)		100.2
	glass	3	42.37(9)	0.027(5)	2.25(5)		18.7(2)	8.1(1)	11.18(5)	15.2(2)	0.27(3)	0.03(2)		98.1
CHV-E349	cpx	4	51.5(3)		1.1(2)	0.005(6)	23.5(2)	15.7(3)	4.0(3)	4.1(1)	0.09(2)	0.54(1)		100.7
	glass	3	42.37(5)	0.04(2)	2.3(2)	0.03(2)	18.8(2)	8.3(2)	11.14(8)	15.4(2)	0.29(5)	0.04(2)	0.05(2)	98.7
CHV-E421	ol	10	39.77(1)				0.39(3)	45.2(1)	0.03(1)	14.4(1)	0.34(2)	0.37(3)	0.18(1)	100.7
	opx	11	56.4(3)	0.02(1)	0.07(4)		2.5(3)	31.4(5)	0.46(7)	8.8(1)	0.35(2)	0.78(7)	0.06(1)	100.9
	glass	10	53.1(3)	0.65(3)	0.67(7)	0.26(2)	12.7(2)	11.8(1)	9.7(1)	11.4(2)	0.34(3)	0.46(3)		101.0
Bulk CHV-E154_,155,156, 157[b]	cpx	20	50.9(2)	0.031(5)	1.29(8)	0.006(4)	23.4(1)	15.2(3)	4.6(3)	4.8(2)	0.098(2)	0.29(6)	0.007(3)	100.6
	glass	20	41.6(1)	0.32(2)	2.38(3)	0.051(1)	18.26(5)	7.89(5)	11.41(4)	15.84(9)	0.30(1)	0.020(6)	0.010(7)	98.1
CHV-E281	ol	5	39.8(3)		0.02(1)		0.35(3)	46.0(8)	0.029(9)	14(1)	0.33(4)	0.31(3)		100.8
	pig	8	55.7(2)		0.07(3)		5.4(8)	28.0(5)	0.46(4)	10.0(6)	0.37(2)	0.51(6)		100.5
	cpx	10	53.9(3)		0.16(3)		17(1)	20.0(7)	1.25(1)	6.5(4)	0.27(2)	0.79(6)		100.2
	glass	10	49.1(2)	0.04(2)	0.68(1)	0.01(1)	14.7(2)	10.08(1)	11.34(6)	12.4(1)	0.34(3)	0.29(3)		99.0
CHV-E282	ol	5	39.5(2)		0.017(9)		0.34(2)	45.8(8)	0.03(1)	14.6(8)	0.32(4)	0.32(3)		100.9
	pig	10	56.2(2)	0.006(1)	0.06(3)		5.0(9)	29.5(8)	0.55(1)	8.4(2)	0.34(2)	0.63(3)		100.6
	cpx	10	54.3(2)		0.16(3)		16.1(6)	21.3(5)	1.10(9)	6.2(3)	0.27(3)	0.82(6)		100.3
	glass	5	48.9(3)	0.05(3)	0.71(9)		14.78(9)	10.2(2)	11.3(2)	12.4(2)	0.33(4)	0.31(3)		99.1
GPC_866	cpx	10	51.8(4)	0.23(2)	0.57(9)	0.002(3)	22.8(2)	16.1(4)	4.7(5)	3.3(3)	0.11(2)	0.5(2)		100.3
	glass	8	44.6(2)	0.92(5)	2.3(1)	0.27(3)	20.9(2)	9.69(5)	11.4(1)	7.7(3)	0.28(4)	0.05(2)		98.2
YPC_586	cpx	11	52.7(6)	0.29(3)	0.68(6)	0.010(9)	22.4(2)	14.8(5)	5.8(9)	5.0(2)	0.01(1)	0.36(8)		100.1
	glass	10	43.8(2)	1.18(5)	2.7(2)	0.38(2)	19.1(1)	8.1(2)	12.0(1)	11.8(2)	0.02(3)	0.03(3)		97.0
CHV-E227	pl	10	45.9(4)	0.70(9)	0.17(6)	0.03(2)	18.3(3)	0.40(6)	33.9(4)	0.22(5)	0.02(2)			99.7
	cpx		48(2)	0.06(2)	5(1)		22.5(4)	16(1)	7(2)	2.6(2)	0.12(2)	0.3(1)		100.1
	glass	5	42.1(2)	0.36(4)	9.6(4)	0.07(2)	16.2(2)	9.7(1)	12.4(1)	9.1(1)	0.31(3)	0.04(4)		99.8
CHV-E284	pl	5	45.0(2)	0.17(5)	0.16(5)	0.01(1)	19.3(2)	0.45(3)	34.5(3)	0.21(6)	0.02(2)	0.005(7)		99.9
	cpx		48(2)	0.01(1)	4.3(9)		22.5(2)	15.9(9)	6(2)	2.6(3)	0.12(2)	0.5(2)		100.2
	glass	5	42.2(2)	0.09(2)	9.6(2)	0.02(1)	16.4(2)	9.87(9)	12.14(6)	8.9(2)	0.28(4)	0.04(2)		99.5

Errors (1σ) standard deviation of the average of n analyses, given in brackets

[a]All compositional data were filtered by exclusion of values that diverged by > 2σ from the median of all analyses n of one phase, thereby analyses on fractures or holes, which resulted in bad totals, could be excluded in a statistically meaningful way. Individual measurements are reported in Supplementary Table S1

[b]Individual compositions of CHV-E155–157 (abbreviated as CHV-E15) can be found in Supplementary Table S3

Potassium in medium resolution mode

Potassium, which is very incompatible in clinopyroxene, was analyzed using LA-ICP-MS in medium resolution mode to resolve isobaric interferences with Ar isotopes. An ablation rate of 20 Hz was chosen and NISTSRM610 was used as a standard and Ca for internal standardization. Two experiments with CHV-6C starting material (CHV-E346, 349) and two experiments with CHV-6B starting material (CHV-E227, CHV-E284) were analyzed (Supplementary Table S2). We only analyzed clinopyroxene, because other minerals were too small for the chosen spot sizes of 120 µm, which were necessary to attain a signal higher than background (Supplementary Tables S2, 3, 4). During each analysis both, background and peak, were measured for 40 s with a washout time of 25 s. Isotopes ^{29}Si, ^{39} K and ^{43}Ca were analyzed during the session. NISTSRM612, 614 and USGS BIR-1G reference materials were measured each ~ 15 LA-ICP-MS spots (secondary reference materials) to assess the quality of the K-measurements (Supplementary Table S4).

The averages of most analyzed trace elements diverge by < 5% from literature values. Especially for the high-resolution measurements of K in clinopyroxene the reproduction of K abundances in the reference material measured as unknowns (NISTSRM612, NISTSRM614: < 5% deviation from GeoRem preferred values; Supplementary Table S4) is good evidence for the quality of the measurements. Data reduction for LA-ICP-MS was done using the Glitter software package (Jackson 2001).

Attainment of equilibrium

The attainment of equilibrium during our experiments is evaluated based on chemical compositions of the run products and textures. We chose run durations that are similar to durations reported in previous studies investigating trace element partitioning (e.g., Leitzke et al. 2016; Klemme et al. 2006; Table 2). Low standard deviations of major and trace elemental analyses of minerals and quenched glasses suggest the attainment of equilibrium between minerals and melt. Note that this excludes the zoned clinopyroxene of experimental run products CHV-E227 and 284, and clinopyroxene with quench overgrowth rims in the high-P experiments (Fig. 1c). Quench rims were avoided during analyses.

The Fe–Mg exchange coefficients (K_D^{Fe-Mg}) between unzoned clinopyroxene and melt in this study, another means to assess the attainment of equilibrium (Putirka 2008), ranges between 0.15 and 0.29, which is in excellent agreement with previous studies (Shepherd et al. 2022 and references therein). K_D values increase with increasing melt CaO, decreasing melt SiO_2, logfO_2, pressure, and temperature , in accordance with previous observations (Bédard 2010). Moreover, the sub- to euhedral morphologies of crystals in our runs also indicate equilibration. In the runs where olivine is present, olivine-melt K_D^{Fe-Mg} values also indicate equilibration ($K_D^{Fe-Mg} = 0.33$: experiments using the CHV-PiM starting material; $K_D^{Fe-Mg} = 0.26$: experiments with CHV-10, Roeder and Emslie 1970; Mallik et al. 2019; Zhang et al. 2023). In this context, it is important to note that K_D^{Fe-Mg} is almost constant at about 0.3 in terrestrial basaltic systems, but it can vary significantly at lunar conditions (Krawczynski and Grove 2012). This is particularly relevant for runs with starting material CHV-6B, which has high Ti contents (7.46 wt% TiO_2) and it is known that highTi reduces the activity of FeO in the melt (Krawczynski and Grove 2012).

Furthermore, $D^{cpx-melt}$ at 1200 °C and at atmospheric pressure were determined in multiple runs (runs CHV-E154, 155, 156, 157 with starting material CHV-6C, Table 2). Major and trace element compositions are in excellent agreement (cf. Table 4, below and Supplementary Material Table S1–3), which is another strong argument for the attainment of equilibrium during the experimental runs.

Iron loss

A few 1-atm pressure experiments show minor Fe loss (1–2%) which was identified in the mass balance calculation (Table 2). The high-P experiments show 5–7% of Fe-loss, as Fe is known to alloy with the Pt capsule, and our graphite liners (see experimental methods, above) apparently did not completely prevent Fe loss to the metal. However, the analyses of quenched melt and crystals show that phases are homogeneous throughout the run (Fig. 1c, Figure S2), and this enabled us to analyze trace element concentrations in both phases and to determine $D^{cpx-melt}$.

Results

Macroscopic observations and EPMA analysis

The major element compositions of the analyzed phases are given in Table 3. Figure 1 shows back-scattered electron images of typical run products of our 1-atm and high-P experiments. Modal proportions were determined by mass balance calculations using the phases' major element compositions. In the following we describe the macroscopic observations of the run products, sorted according to the starting material.

Starting material CHV-6B

Two experiments were conducted using starting material CHV-6B at atmospheric pressure. These were run at 1200 °C and fO_2 of IW–1 (CHV-E284) and IW–2 (CHV-E227:

Table 4 Trace element partition coefficients between silicate minerals (clinopyroxene: cpx, pigeonite: pig, orthopyroxene: opx, plagioclase: pl, and olivine: ol) and melt, trace elements in all phases were analyzed with LA-ICP-MS

Run ID	T (°C)	ΔIW	Li	Si	Ca	K	Sc	Ti	V	Cr	Mn	Co
$D^{cpx-melt}$												
CHV-E424	1240	IW	0.11(3)[a]	1.17(2)	1.127(9)		2.0(2)	0.32(5)	3.4(7)	6(1)	0.36(2)	0.57(2)
CHV-E154	1200	−1	0.08(3)	1.22(5)	1.283(7)		4.0(3)	0.54(9)	10(2)	14(5)	0.37(2)	0.90(5)
CHV-E155	1200	−1	0.07(2)	1.28(2)	1.279(7)		4.0(5)	0.54(7)	9(3)	13(5)	0.38(2)	0.84(5)
CHV-E156	1200	−1	0.06(1)	1.23(3)	1.279(7)		4.1(6)	0.58(7)	11(4)	17(10)	0.36(3)	0.89(8)
CHV-E157	1200	−1	0.066(9)	1.22(2)	1.27(1)		4.7(6)	0.61(3)	14(4)	26(10)	0.33(2)	0.86(4)
Bulk_CHV-E15	1200	−1	0.070(5)	1.24(1)	1.281(3)	0.0035(2)	4.2(2)	0.57(2)	11(1)	18(3)	0.360(8)	0.87(2)
CHV-E346	1200	−1				0.005(6)						
CHV-E349	1200	−1				0.0035(2)						
CHV-E281	1200	−1	0.26(4)	1.1(1)	1.22(6)		1.16(8)	0.27(3)	3.7(2)	2.7(2)	0.8(1)	1.1(2)
CHV-E282	1200	−1	0.28(2)	1.10(4)	1.10(5)		0.96(6)	0.21(1)	3.6(3)	2.6(1)	0.75(3)	1.29(6)
YPC_586	1310	+1.5	0.15(2)	1.19(2)	1.17(1)		1.76(8)	0.30(3)	2.5(2)	12(1)	0.41(3)	0.9(1)
GPC_866	1310	+1.5	0.14(2)	1.13(2)	1.09(1)		1.5(1)	0.25(2)	2.4(2)	12(2)	0.37(2)	2.0(7)
CHV-E227	1200	−2				0.0008(4)						
CHV-E284	1200	−1				0.0030(8)						
$D^{pig-melt}$												
CHV-E281	1200	−1	0.13(2)	0.8(2)	0.43(1)		0.39(2)	0.10(6)	1.40(1)	1.3(2)	0.73(7)	1.10(7)
CHV-E282	1200	−1	0.217(1)	1.111(3)	0.29(3)		0.46(4)	0.102(8)	2.0(3)	1.88(7)	0.85(2)	1.93(7)
$D^{opx-melt}$												
CHV-E421	1270	IW	0.18(1)		0.22(1)		0.42(1)	0.104(6)	0.91(4)	1.79(4)	0.98(2)	1.37(4)
$D^{pl-melt}$												
CHV-E227	1200	−2	0.26(6)	1.079(3)	1.08(5)		0.012(3)	0.018(4)		0.013(4)	0.024(3)	0.031(2)
CHV-E284	1200	−1	0.27(3)	1.107(4)	1.12(1)		0.010(3)	0.010(2)			0.026(2)	0.035(7)
$D^{ol-melt}$												
CHV-E421	1270	IW	0.028(9)	0.16(2)	0.032(3)		0.055(7)	0.014(1)	0.12(1)	0.25(3)	0.15(2)	0.21(3)
CHV-E281	1200	−1	0.33(1)	0.81(3)	0.0219(8)		0.18(2)	0.015(5)	1.0(2)	1.04(5)	0.82(1)	3.72(4)
CHV-E282	1200	−1	0.30(1)	0.81(5)	0.024(2)		0.18(2)	0.015(6)	0.9(1)	1.03(6)	0.867(1)	4.3(1)

Ni	Cu	Zn	As	Rb	Sr	Y	Zr	Nb	Mo	Cs	Ba
1.50(1)					0.090(6)	0.21(3)	0.11(4)	0.003(1)	0.12(4)		0.000919(7)
1.3(2)	1.3(5)[b]		0.3(1)	0.106(2)	0.096(7)	0.33(5)	0.31(8)	0.008(3)	0.6(3)		0.0011(1)
1.8(4)		1.9(5)[b]	2(1)[b]		0.096(7)	0.34(3)	0.30(5)	0.009(2)	0.6(2)		0.002(2)
1.3(2)			0.4(1)		0.095(7)	0.33(4)	0.32(6)	0.008(2)	0.7(4)	0.146(9)	0.0012(5)
1.1(2)					0.090(4)	0.33(2)	0.34(2)	0.011(2)	0.8(2)		0.0014(3)
1.36(9)	1.3(5)[b]	1.9(5)[b]	0.35(10)	0.106(2)	0.095(2)	0.33(1)	0.32(2)	0.0090(8)	0.66(9)	0.146(9)	0.0015(3)
1(1)	0.2(2)				0.05(1)	0.21(2)	0.03(2)	0.01(1)			0.01(1)
2.2(9)			1.1(2)		0.034(2)	0.165(9)	0.018(2)	0.0012(3)	2(1)		0.0007(1)
		0.25(3)	0.9(3)	0.010(3)	0.118(6)	0.25(3)	0.14(3)	0.019(1)	0.04(1)	0.009(3)	0.011(5)
		0.23(2)	1.9(4)		0.107(2)	0.19(2)	0.09(2)	0.003(1)	0.037(5)		0.0015(1)
0.7(9)		0.3(1)	1.4(7)		0.0131(7)	0.062(4)	0.016(2)	0.0063(4)			0.0047(8)
4(1)	1(1)	1.6(5)			0.0028(3)	0.045(4)	0.007(5)	0.002(1)			0.002(1)
3.0(1)	1.38		2(1)		0.0022(5)	0.042(5)	0.0039(5)	0.0020(6)	0.22(4)		0.00275(4)
	6(4)[b]	4(1)[b]	3.2(9)[b]		1.21(4)	0.008(5)	0.007(4)	0.005(5)			0.15(2)
			2.3(3)[b]		1.21(7)	0.004(3)	0.002(2)	0.003(4)	0.64(7)		0.13(2)
0.46(6)		0.489	0.16(7)		0.00031(9)	0.0050(4)	0.00056(8)	0.00015(5)	0.022(4)	0.0037(2)	0.000220(3)
7(9)		0.35(6)			0.0009(2)	0.006(1)	0.01(1)	0.0010(1)			0.0010(4)
11(4)	0.7(1)					0.0056(8)	0.0016(8)	0.0003(2)			

La	Ce	Pr	Nd	Sm	Eu	Gd	Tb	Dy	Ho	Er
0.044(9)	0.07(1)	0.11(2)	0.14(3)	0.20(4)	0.16(2)	0.22(2)	0.22(3)	0.22(3)	0.22(3)	0.21(4)

Table 4 (continued)

La	Ce	Pr	Nd	Sm	Eu	Gd	Tb	Dy	Ho	Er
0.07(1)	0.12(2)	0.17(3)	0.22(3)	0.31(6)	0.19(3)	0.35(6)	0.36(5)	0.36(6)	0.35(6)	0.34(5)
0.073(9)	0.12(1)	0.17(2)	0.23(2)	0.32(4)	0.19(3)	0.36(4)	0.37(3)	0.37(3)	0.35(4)	0.34(3)
0.073(7)	0.12(1)	0.17(2)	0.22(2)	0.32(4)	0.21(3)	0.35(4)	0.36(4)	0.36(4)	0.35(4)	0.33(4)
0.075(2)	0.119(2)	0.164(1)	0.22(2)	0.31(3)	0.182(8)	0.35(3)	0.38(2)	0.36(2)	0.35(3)	0.33(2)
0.073(2)	0.118(4)	0.167(7)	0.222(8)	0.31(1)	0.192(7)	0.35(1)	0.37(1)	0.36(1)	0.35(1)	0.34(1)
0.03(1)	0.05(1)	0.07(2)	0.10(2)	0.15(2)	0.08(2)	0.20(4)	0.21(2)	0.22(2)	0.22(3)	0.23(3)
0.016(2)	0.027(2)	0.046(3)	0.067(9)	0.10(2)	0.054(6)	0.14(1)	0.15(1)	0.16(1)	0.17(1)	0.17(1)
0.06(1)	0.09(1)	0.13(2)	0.17(3)	0.22(1)	0.21(2)	0.27(4)	0.27(2)	0.28(3)	0.27(2)	0.26(4)
0.042(4)	0.066(9)	0.09(1)	0.12(1)	0.17(2)	0.16(1)	0.20(2)	0.21(2)	0.21(2)	0.21(3)	0.20(2)
0.0101(7)	0.0122(1)	0.018(2)	0.024(3)	0.037(6)	0.029(4)	0.048(7)	0.054(5)	0.064(6)	0.064(5)	0.067(6)
0.0021(6)	0.004(1)	0.004(1)	0.008(2)	0.011(3)	0.009(3)	0.03(1)	0.030(3)	0.038(4)	0.047(6)	0.056(5)
0.0012(3)	0.003(2)	0.004(2)	0.004(1)	0.012(6)	0.006(1)	0.028(3)	0.029(4)	0.036(4)	0.043(4)	0.05(1)
0.026(4)	0.021(3)	0.021(6)	0.018(3)	0.017(7)	0.64(3)	0.016(5)	0.02(1)	0.009(3)	0.010(5)	0.012(5)
0.019(5)	0.017(6)	0.016(4)	0.014(5)	0.016(4)	0.57(4)	0.018(3)	0.009(5)	0.009(6)	0.007(3)	0.004(5)
0.00014(6)	0.00022(7)	0.0004(1)	0.0007(4)	0.0018(5)	0.0010(2)	0.004(1)	0.0036(9)	0.0048(6)	0.0048(6)	0.0066(1)
0.0006(4)	0.0009(5)	0.002(1)	0.0014(5)	0.00096	0.004(2)	0.006(3)	0.002(1)	0.005(1)	0.007(2)	0.010(2)
0.000182(2)			0.0006(3)		0.004(1)		0.0021(4)	0.0038(6)	0.005(1)	0.007(3)

Tm	Yb	Lu	Hf	Ta	Pb	Th	U
0.19(3)	0.20(3)	0.20(3)	0.25(8)	0.007(4)		0.005(2)	0.005(2)
0.32(5)	0.31(5)	0.33(5)	0.7(2)	0.03(1)		0.011(3)	0.011(3)
0.33(3)	0.33(4)	0.35(3)	0.6(1)	0.027(1)	0.48(50)	0.014(4)	0.012(4)
0.31(4)	0.32(4)	0.33(3)	0.7(1)	0.03(1)	3(2)[b]	0.013(3)	0.011(3)
0.33(3)	0.310(6)	0.34(2)	0.75(5)	0.039(6)		0.015(2)	0.011(1)
0.32(1)	0.32(1)	0.34(1)	0.68(4)	0.031(4)	0.48(50)	0.013(1)	0.0114(9)
0.22(2)	0.21(4)	0.21(3)	0.07(2)	0.01(2)	0.4(6)	0.01(2)	0.01(2)
0.17(1)	0.168(9)	0.171(9)	0.040(4)	0.0013(4)		0.0019(4)	0.0021(1)
0.25(5)	0.25(3)	0.25(3)	0.28(5)	0.04(2)	0.04(1)	0.03(1)	0.020(1)
0.19(2)	0.18(2)	0.19(2)	0.20(5)	0.010(5)	0.035(1)	0.006(2)	0.0039(9)
0.066(6)	0.081(8)	0.080(4)	0.018(3)	0.0076(8)	0.1(2)	0.0065(5)	0.0082(7)
0.067(9)	0.07(1)	0.073(6)	0.008(3)	0.0012(2)	0.02(4)	0.001(1)	0.0010(8)
0.059(7)	0.06(1)	0.076(4)	0.009(3)	0.003(2)		0.0007(6)	0.001(1)
0.008(4)	0.010(5)	0.006(3)	0.006(4)	0.006(2)	5(4)[b]	0.006(4)	0.009(9)
0.006(6)	0.005(1)	0.003(2)	0.004(2)	0.01(1)		0.002(4)	0.002(3)
0.0071(7)	0.0084(7)	0.010(1)	0.0007(5)	0.00015(6)		0.0002(3)	0.00003(1)
0.013(3)	0.018(4)	0.023(3)	0.005(3)	0.002(2)	0.3(4)	0.00032(2)	0.0007(4)
0.012(3)	0.016(3)	0.023(2)	0.003(3)	0.0011(1)			0.00017(5)

[a]Errors on $D^{mineral-melt}$ were calculated by propagating the relative standard errors of the concentrations (Supplementary Material Methods). Melt contamination in a mineral analysis was monitored and filtered by checking carefully for elevated Rb and Cs, both being elements which are extremely incompatible in all analyzed silicate minerals

[b]Maximum partition coefficients due to evaporative loss of elements from the melts during the run

Fig. 1a). Both runs contain large homogeneous glassy areas (73–75%), with a basaltic composition. Mineral phases are sub- to anhedral large clinopyroxene crystals (500–1000 µm: 20%) and acicular laths of plagioclase (4%). The clinopyroxenes are sector zoned ($Wo_{47-51}En_{45-49}Fs_{4.5-4.3}$), and were not analyzed for trace elements because zonation is an indicator for local disequilibrium. Nevertheless, plagioclase (pl) crystals are homogeneous with 93.5 (CHV-E227) and 98 mol% (CHV-E284) anorthite content and hence $D^{pl-melt}$ were calculated.

Starting material CHV-6C

Three 1-atm experimental runs (42, 84, 120, Table 2) including seven individual experiments (CHV-E154, 155, 156, 157 and 346, 349) were run at identical experimental

conditions. Further, one experiment was conducted at higher T (CHV-E424), and two experiments at high-P (YPC 586, GPC 866). Experiments of run 42 (CHVE-154, 155, 156, 157: Fig. 1b) were run at atmospheric pressure, 1200 °C, and an fO_2 corresponding to ΔIW–1. These runs were used to determine trace element concentrations and $D^{mineral-melt}$ (for details, see Supplementary Material). Experiments CHVE-346 and 349 were replicate runs to analyze K. To assess the effect of temperature, one experiment (CHVE-424) was conducted at 1240 °C and an fO_2 of IW. Two experiments were conducted at high-P of 1.5 GPa and 1310 °C in graphite-lined Pt- capsules, which sets an upper fO_2 limit of ~ ΔIW + 1.5 (Medard et al. 2008). The run temperature was increased in these experiments, compared to the 1-atm experiments, because of the P-effect on the liquidus. The clinopyroxene crystals in all runs including starting material CHV-6C are homogeneous and close to diopside ($Wo_{46-49}En_{44-47}Fs_{5-8}$, Supplementary Figure S1), melt fractions are > 50% and melts are homogeneous (Supplementary Table S3). Quench rims were observed only around clinopyroxene in the high-P runs (YPC568: Fig. 1c, GPC866: Supplementary Figure S2), which were avoided during major and trace element analyses. In contrast to 1-atm pressure experiments, we did not average the results of the high-P experiments, because we observed different degrees of Fe-loss (Table 1, 5–7%), affecting melt and clinopyroxene composition and in turn affecting partition coefficients.

Starting material CHV-10

Two experiments (CHVE-281, CHVE-282) were conducted using starting material CHV-10 at atmospheric pressure, 1200 °C, and an fO_2 of IW–1. The experiments contain 71–72% of homogeneous glass, small (10–20 µm) olivine grains (1.6–2%), and augitic clinopyroxene and pigeonite intergrowth aggregates of 100–200 µm diameter. Experiment CHVE-282 contains two large grains of clinopyroxene and pigeonite (1000 µm in size: Fig. 1d). $D^{mineral-melt}$ were determined for all phases. Due to its size (~ 15 µm), pigeonite in run product CHVE-281 was measured only once, which inhibits a reasonable error assessment, whereas pigeonites in run CHVE-282 could be measured multiple times.

Starting material PiM

One experiment was conducted with the starting material CHV-PiM (CHV-E421, Table 2) at 1270 °C at an fO_2 of IW, yielding small (~ 50 µm sized) crystals of olivine (7%) and enstatite ($Wo_5En_{82}Fs_{13}$: 5%).

Trace element compositions and partition coefficients

Partition coefficients between minerals and co-existing silicate melt were determined by dividing the trace element concentrations in the mineral by the trace element concentration in the melt ($D^{mineral-melt} = c_{mineral}/c_{melt}$), and the resulting partition coefficients are compiled in Table 4. The analytical results of all minerals and quenched melts are given in the Supplementary Material Tables S2 and S3. Element concentrations were determined by measuring crystals and glass (homogeneous quenched melt) multiple times, when crystal size was large enough.

Our dataset contains $D^{mineral-melt}$ for 36 trace elements for clinopyroxene, plagioclase, pigeonite, orthopyroxene, and olivine at lunar conditions, which complements the existing datasets (e.g., Dygert et al. 2013, 2014, 2020; Sun and Liang 2013; Leitzke et al. 2016; Snape et al. 2022). Figure 2 depicts all of our new $D^{mineral-melt}$, together with selected literature data and includes a detailed section of the D_{REE}.

Clinopyroxene, pigeonite, and orthopyroxene

Monovalent and divalent cations show similar partition coefficients for high-Ca and low-Ca pyroxenes (Fig. 2a, b). Potassium, Rb, and Cs are very incompatible in pyroxenes. $D^{mineral-melt}$ in runs at 1-atm are about one magnitude higher than in high-P experiments. Nevertheless, Rb and Cs $D^{cpx-melt}$ are most reliable in the high-P experiments ($D^{cpx-melt} = 0.01$ and 0.009, respectively; Fig. 2a). We note that $D^{cpx-melt}$ for Cs, Rb, K, Mn, Pb, and also Cu, Zn, and As at atmospheric pressure are potentially too high because these elements are moderately to highly volatile (Sossi et al. 2019) and may have escaped from the experimental melts during the runs. Hence, we conclude that these $D^{mineral-melt}$ for 1-atm experiments must be considered maximum values but they are nevertheless reported in Table 3. In Fig. 2, Li, K, Rb, Cs, Mn, and Pb are shown for comparison. In clinopyroxene, Li, Ba, Sr, As, U, and Th are the only elements, which become less incompatible with increasing pressure (e.g., $D_{Li\ high\ P} = 0.15$, $D_{Li\ 1\text{-}atm} = 0.07$; Table 4). Potassium $D^{cpx-melt}$ are between 0.003–0.005 and should be regarded as maximum values, since the concentrations of K in analyzed clinopyroxenes are near the detection limit.

$D^{cpx-melt}$ for monovalent and divalent ions affected by volatile loss are reliable in high-P runs (e.g., $D_{Pb} = 0.037$) as evaporation is not an issue in these runs. Compared to literature, our partition coefficients are similar or slightly lower. Divalent cations (Mn, Co, Ni, Sr, Ba and eventually Cu, Zn, Pb in high-P experiments) are the least incompatible in clinopyroxene (Fig. 2a, Table 4). $D^{cpx-melt}$ for Mn, Co and Ni are about one order of magnitude smaller than those

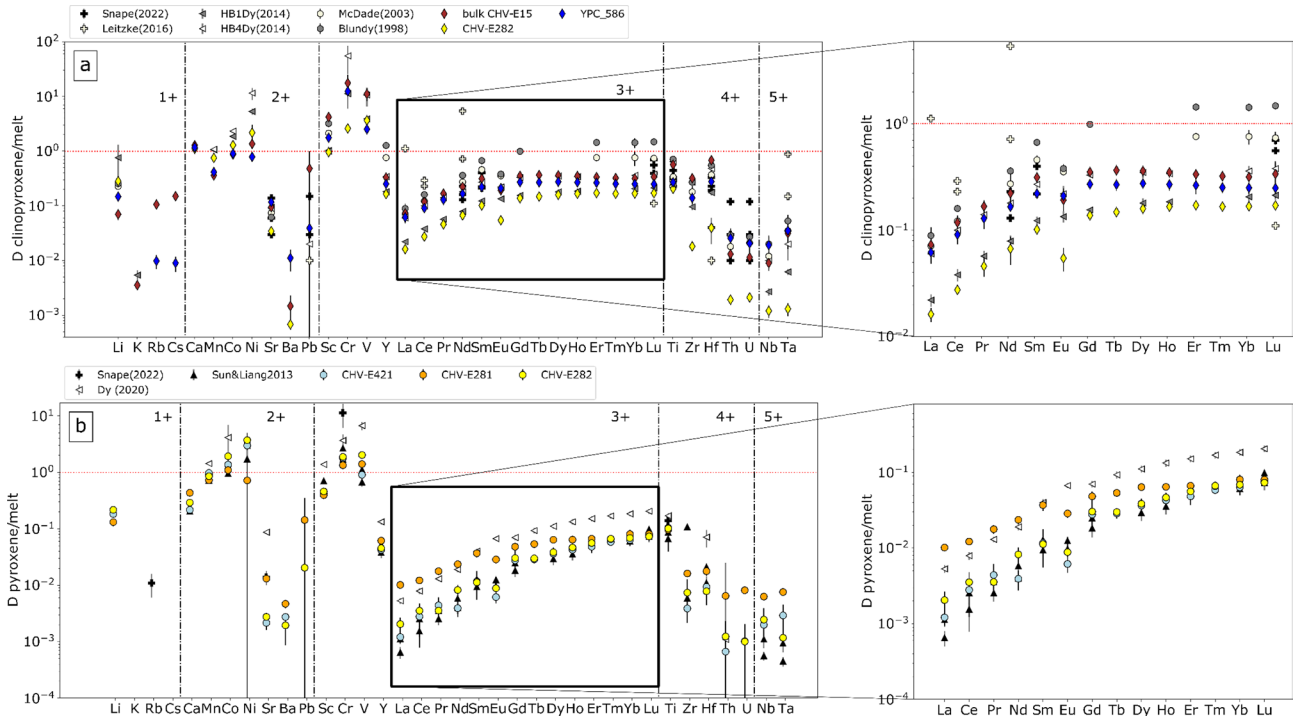

Fig. 2 Experimental and literature $D^{mineral-melt}$ sorted by mineral and valence (1+, 2+, 3+, 4+, 5+) of the trace elements plus a detailed section showing D_{REE}. Red dotted lines correspond to $D^{mineral-melt} = 1$. **a** $D^{cpx-melt}$ from this study (brown diamond: CHV-E15, yellow diamond: CHV-E282, and high-P experiment in blue: YPC586). high-Ca pyroxene (RD-L-PC16_2/_3a) from Snape et al. (2022), T1_20Ti and T1_0TiREE at IW–1.6 from Leitzke et al. (2016), partition coefficients of unzoned high-Fe clinopyroxenes at 1050 and 1150 °C from Dygert et al. (2014). **b** $D^{px-melt}$ from this study (colored dots are pigeonite CHV-E281/82 and orthopyroxene CHV-421) plotted with literature data (orthopyroxene A15GG210 and A15Y from Sun and Liang 2013; pigeonite TJ-TWM-S9_2a and TJ-TWM-S9_2b from Snape et al. 2022, pigeonite Eu14-17 from Dygert et al. 2020), **c** $D^{pl-melt}$ of this study (CHV-E227, 284) and literature data (Snape et al. 2022: RD-L-GM25_12 and TJ-TWM-S9_2a; Dygert et al. 2020: Eu1412a, Eu1413, Eu1417; Aigner-Torres et al. 2007: 35 and 36 where fO_2 = IW and in air, respectively), **d** $D^{ol-melt}$ from this study (CHV-E281/82, and 421) with literature data (Chen et al. 2022: 15016-Ol10 and 15647-Ol6, Dygert et al. 2020: Eu14-12a, Eu14-17)

reported by Dygert et al. (2014) for Fe-rich clinopyroxenes (cf. Supplementary Figure S1).

Our $D^{cpx-melt}$ for Mn, Co, and Ni overlap with data from Dygert et al. (2014) and these elements are compatible in clinopyroxene ($D^{cpx-melt} > 1$). Chromium and V are especially sensitive to oxygen fugacity. Their high partition coefficients ($D^{cpx-melt}$ for Cr = 6–17 and $D^{cpx-melt}$ for V = 2–10, respectively) agree with data of experimental $D^{mineral-melt}$ at reducing conditions (Mallmann et al. 2021; Shepherd et al. 2022). Their compatibility decreases with decreasing Ca content of pyroxene (Fig. 2a, b; Supplementary Table S3). The $D^{mineral-melt}$ of Ni in pyroxenes decrease from high-Ca pyroxene towards low-Ca pyroxene (Fig. 2a, b). Compared with $D^{cpx-melt}$ determined at terrestrial conditions (i.e., high fO_2, Blundy et al. 1998; McDade et al. 2003), the pattern of D_{REE} is very similar. Nevertheless, lunar $D^{cpx-melt}$ are lower than terrestrial $D^{cpx-melt}$ (Fig. 2a; Blundy et al. 1998 and McDade et al. 2003) but generally agree with the data of Dygert et al. (2014). Snape et al. (2022) only published $D^{mineral-melt}$ for Sr, Pb, Rb, Sm, Nd, Lu, Hf, U, and Th which are all similar or lower than our data. D_{REE} for low-Ca pyroxene have a similar pattern to high-Ca pyroxene but D_{REE} are generally up to two magnitudes lower (e.g., D_{Pr}: 0.1 in cpx, 0.004 in opx; Fig. 2b, Table 4). $D^{pigeonite-melt}$ of CHV-E281 are higher, than CHV-E282 and lower than $D^{cpx-melt}$, which could indicate a mixed analysis or small-scale zonation (Figs. 1d, 2b). $D^{cpx-melt}$ of tetravalent high-field strength elements (Ti, Zr, Hf) of our study are highest in clinopyroxene CHV-E15 (0.5, 0.3, and 0.7 respectively) and lowest in clinopyroxene of CHV-E282 (0.21, 0.018, 0.0395), whereas Th, U, Nb, and Ta are more incompatible than in all previous studies (Fig. 2a). $D^{cpx-melt}$ are systematically lower in the high temperature experiment at ambient pressure (CHV-E424) than in both high-P experiments. HFSE show a similar partitioning behavior in low-Ca pyroxenes compared with high-Ca pyroxenes, where Ti is the most compatible HFS element ($D^{px-melt} = 0.01$; Fig. 2b), followed by D_{Zr} and $D_{Hf} > 0.001$.

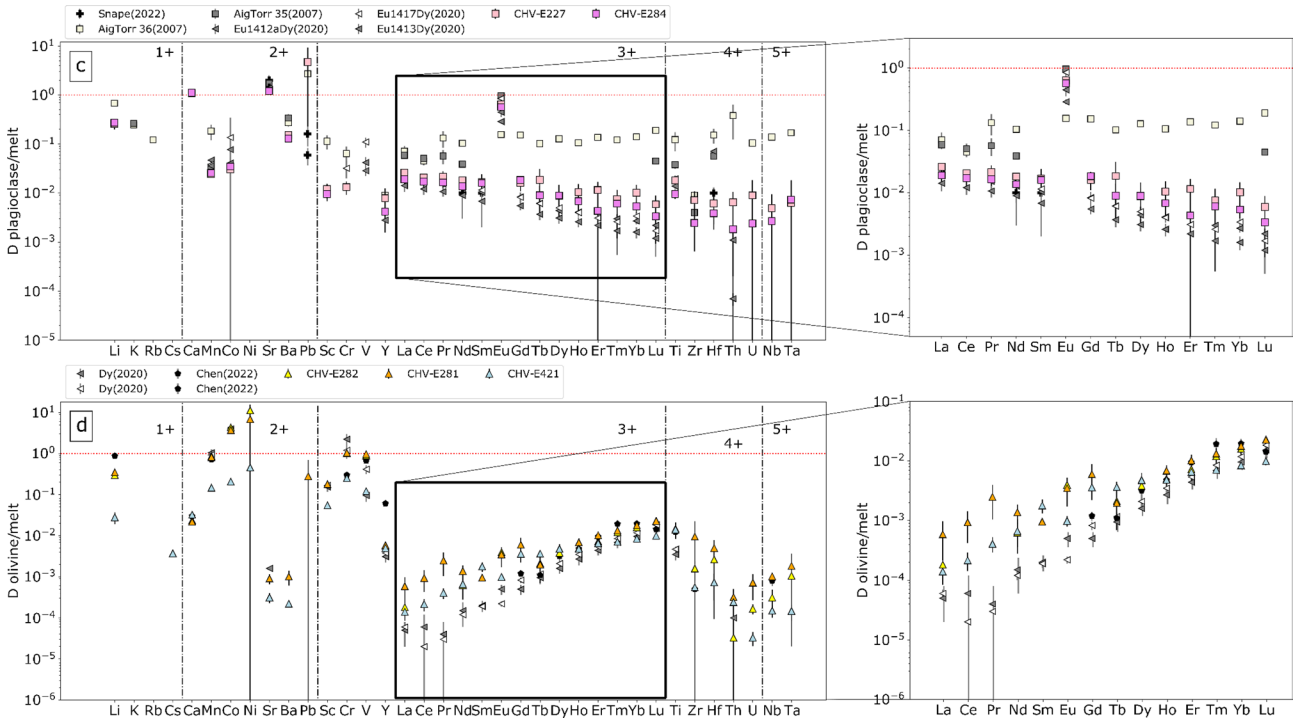

Fig. 2 (continued)

Plagioclase

Monovalent ions are slightly incompatible in plagioclase. Lithium is the least incompatible element in plagioclase ($D^{pl-melt} = 0.26$; Fig. 2c; Table 4) and $D^{pl-melt}$ for divalent elements Mn, Co, and Ni agree with those of Dygert et al. (2020). The high $D^{pl-melt}$ for Pb could indicate Pb-loss and the value has to be taken with caution. $D^{mineral-melt}$ of Sc, V, Cr, and Y are lower than literature values (Fig. 2c). In plagioclase, all REE are very incompatible ($D < 0.01$; Fig. 2c) with the exception of Eu ($D_{Eu} = 0.57–0.64$), which can enter the plagioclase structure as Eu^{2+} under reduced conditions (e.g., Dygert et al. 2020). The data show, that the proportion of Eu^{2+} entering plagioclase increases with decreasing fO_2 (at ΔIW–2 $D^{pl-melt} = 0.64$). In experiments performed in air (Aigner-Torres et al. 2007), the D_{Eu} is very similar to other REE (Fig. 2c). In plagioclase, $D^{pl-melt}$ of REE as well as tetravalent and pentavalent ions are similar to Dygert et al. (2020) and Snape et al. (2022) and lower than the values of Aigner-Torres et al. (2007) (Fig. 2c).

Olivine

Experimental $D^{ol-melt}$ (e.g., CHV-E281, Table 3) have large propagated uncertainties. This results mainly from very low concentrations of the trace elements in theolivine crystals. Small crystal sizes allowed not more than four analyses per olivine grain (Supplementary Table S4). The data underlines, that monovalent ions are moderately to highly incompatible in olivine (Fig. 2d). $D^{ol-melt}$ of divalent ions scatter across up to more than one magnitude between the experiments at different temperatures and starting materials (CHV-E281/282 and CHV-E421; Fig. 2d, Table 2). The divalent elements Mn, Co, and Ni in experiments CHV-E281/82 range from moderately incompatible to compatible, whereas they are incompatible in experiment CHV-E421 (e.g., $D_{Co} = 3.72$ and 0.21, respectively; Fig. 2d). Strontium, Ba, and Pb are very incompatible in olivine ($D^{mineral-melt} < 0.01$). D_{Pb} for olivine must be regarded as a maximum value. Scandium, Cr, V, and Y $D^{ol-melt}$ of our experiments are similar to the values of Chen et al. (2022) and Dygert et al. (2020). $D^{ol-melt}$ of light REE are higher, than in the experiments of Dygert et al. (2020). Middle and heavy REE partition coefficients overlap with the data of Chen et al. (2022) for natural lunar olivine-glass pairs and experimental data of Dygert et al. (2020). $D^{ol-melt}$ of the tetravalent and pentavalent elements are very low ($D^{ol-melt} << 0.001$; Fig. 2d, Table 4) and for all elements but Th, the $D^{ol-melt}$ in experiment CHV-E421 are lower than in experiments CHV-E281 and 282.

Controls on $D^{mineral-melt}$

The effects of pressure, temperature, mineral and melt chemistry on trace element partitioning are correlated (Blundy and Wood 1994; Wood and Blundy 1997; Hill et al. 2000, 2011; Prowatke and Klemme 2006a) and hard to disentangle.

As such, the applicability of predictive trace element partitioning models (e.g., Sun and Liang 2012, 2013; Dygert et al. 2014) is often limited within their calibration range (cf. Supplementary Figures S3, S4, S5). The compatibility of a trace element with a mineral depends on the size of a crystal structural site, the charge of the element, and the bond force (Goldschmidt 1937). The size of the crystal structural site itself depends on pressure and temperature: At high pressures, a site will be compressed, meaning that the $D^{mineral-melt}$ of most trace elements will decrease with increasing pressure (McDade et al. 2003). Temperature, has a similar effect, due to a positive entropy of fusion, as temperature increases (Wood and Blundy 1997).

Crystal-chemical controls on partition coefficients are described with the lattice strain model (Brice 1975; Blundy and Wood 1994). The partitioning of an element i with an ionic radius r_i into the crystallographic site with an effective radius r_0 can be described if we know the strain-free partition coefficient (D_0) for $r_i = r_0$ and E = the effective elasticity of the given site:

$$D_i = D_0 \times \exp \frac{\left(-4\pi E N_A \left(\left(\frac{r_0}{2}\right)(r_i - r_0)^2 + \left(\frac{1}{3}\right)(r_i - r_0)^3\right)\right)}{RT} \quad (1)$$

where N_A is the Avogadro's number, T the temperature (K) and R the gas constant (8.3144 J mol^{-1} K^{-1}). The formula describes a near-parabolic dependence of the partition coefficient D_i on the radius r_i of the corresponding site (e.g., M1 and M2 in clinopyroxene). This relation can be used to construct so-called Onuma diagrams using linear least squares regression on E, D_0, and r_0 for isovalent cations (Onuma et al. 1968).

We fitted parabolas for 3+ ions (D_{REE+Y}) for clinopyroxene, pyroxene, plagioclase, and olivine and parabolas for 2+ cations (Mn, Ca, Sr, Eu, Ba) for clinopyroxene and plagioclase. The quality of lattice strain model fits may be taken as an additional evidence for the data quality (Fig. 3; Supplementary Figures S6 and fitting parameters in Supplementary Table S5).

Clinopyroxene

Besides the good fit of the REE + Y on the lattice strain Onuma fit for 3+ ions on M2, we note a slight positive offset of D_{Lu} in all experiments (Fig. 3a), which might originate from the compatibility of Lu with not only the M2, but also the M1 site. In the literature, it has been discussed that HREE can be compatible with both sites. This has been linked to a low Mg# (4.5–52) of the clinopyroxene (Olin and Wolff 2010; Dygert et al. 2014). However, the Mg# of our clinopyroxenes are significantly higher than clinopyroxene in the aforementioned studies (Mg# = 84–90; see also Supplementary Figure S1, where all pyroxenes of this study, including data of Dygert et al. (2014) are plotted) and we conclude that this could be a general feature of Lu in clinopyroxene.

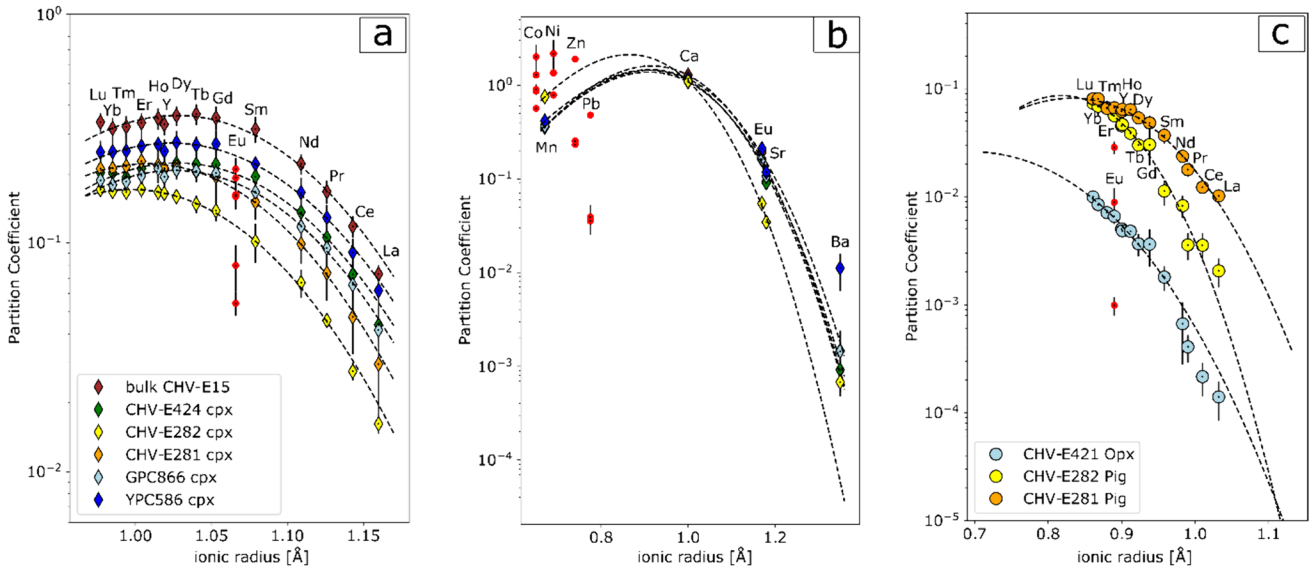

Fig. 3 Partition coefficients for REE + Y and divalent ions (Co, Mn, Ni, Zn, Pb, Ca, Eu, Sr, Ba) for clinopyroxene (**a**, **b**, respectively) and for REE + Y for orthopyroxene and pigeonite (**c**), all plotted as a function of ionic radii (Shannon 1976). Dashed parabolas are lattice strain fits, calculated by linear least squares regression. Red dots correspond to data points, that were not included into the fits (e.g., Eu). Cobalt, Ni, Zn, and Pb are also not included into the fits, as they might enter the M2 side in clinopyroxene. Lattice strain model fits for plagioclase and olivine and the fitting parameters (D_0, r_0, and E) can be found in the supplementary material (Supplementary Figure S6, Supplementary Table S5)

The existing parametrizations for clinopyroxene of Sun and Liang (2012) and Dygert et al. (2014) based on the fraction of Al on the tetrahedral site and the fraction of Mg on the M2 site ($X^{iv}Al$ and $X_{MG}{}^{M2}$) show a clear mismatch to our experimental dataset (Supplementary Figures S3, S4). This underlines the necessity of experimental studies like the one at hand.

Effect of pressure

Our $D^{cpx-melt}$ show that the incompatibility of most trace elements increases with pressure (McDade et al. 2003). This is in general agreement with our observation that $D^{cpx-melt}$ for the REE from our 1-atm pressure experiments are generally higher, than data from the high-P (1.5 GPa) runs for the same starting material (cf. Figs. 2a, 3a, b; e.g., for CHV-E15 and YPC 586 $D_{Gd} = 0.35$ and 0.27, respectively). Sun and Liang (2012) suggest, that the effect of pressure on REE + Y partitioning between clinopyroxene and melt is minor. They argue that the clinopyroxene composition (e.g., Al and Mg in clinopyroxene) and temperature are the major factors controlling trace element partitioning. This might also be true for most of our investigated elements, since compositions of clinopyroxenes in 1-atm and high-P experiments vary slightly due to Fe-loss in the high-P experiments. In contrast, $D^{cpx-melt}$ for elements like Li, Ba, As, Sr, Th, and U are higher at higher P (Table 4), and this is clearly linked to the clinopyroxene composition. For example, for Li $D^{cpx-melt}$ it is known, that at higher pressures (1.5 GPa runs) the jadeite solubility in clinopyroxene increases. This consequently increases the solubility of monovalent elements like Li (McDade et al. 2003), which has a smaller ionic radius (0.76 Å instead of 1.02 Å: Shannon 1976).

Effect of temperature

High temperatures favor the enstatite solubility in diopside, which in turn reduces the size of the M2 site of clinopyroxene (McDade et al. 2003). D_0 of REE linearly decrease with increasing temperature (Sun and Liang 2012), which is also seen in our lattice strain model fit parameters ($D_0 = 0.22$ and 0.36 for 1240 and 1200 °C, respectively; Supplementary Table S5). Hence, the $D^{cpx-melt}$ of elements preferring the M2 sites of clinopyroxene, such as the REE (ionic radius La–Lu: 1.16–1.032), decrease with increasing temperature (Fig. 2a). The effect of temperature strongly enforces the effect of pressure in our experiments, since temperatures in high-P runs were also raised (Table 2), due to the shift of the liquidus at high pressures. The REE partition coefficients of REE + Y and 2+ ions of the high temperature experiment overlap with high-P data (Fig. 3a, b), which underlines the competing effects of temperature, pressure, and composition.

Effect of fO_2

The $D^{cpx-melt}$ (for terrestrial conditions) determined by McDade et al. (2003) and Blundy et al. (1998) are one magnitude higher than $D^{cpx-melt}$ that were determined at much more reducing lunar conditions in this study (Fig. 2a), although P and T at least of our high-P experiments are similar. The low fO_2 of our experiments will mainly influence the oxidation state of Fe (mostly present as Fe^{2+}) and this will influence other major element substitutions linked to Fe. Fe is mainly hosted by the M1 site in the clinopyroxenes of our experiments. If Fe^{2+} substitutes for Mg^{2+} in its low-spin state (radii = 0.72 and 0.61 A, respectively), as suggested by Dygert et al. (2014), the M2 site of clinopyroxene will become larger and hence this site will better accommodate ions that normally partition into the M2 site, such as the REE. The overlap between our data and Dygert et al. (2014), who investigated clinopyroxene which is chemically very distinct from ours (Supplementary Figure S1), could originate from the effect of pressure, which potentially decreases their partition coefficients. Consequently, we suggest, that REE partition coefficients for more Fe-enriched clinopyroxenes at conditions similar to our experiments could be even higher, than our $D^{cpx-melt}$. This highlights the need to understand the correlations between pyroxene chemistry and trace element $D^{mineral-melt}$ (cf. Correlation Matrix Supplementary Figure S7).

Chemical controls on $D^{cpx-melt}$

Most trace element $D^{cpx-melt}$ for trivalent ions correlate well with the proportion of Al on M1 and Al on the tetrahedral side ($X^{IV}Al$) of clinopyroxene (Supplementary Figure S7), because the trace element substitution into the clinopyroxene structure is coupled to Al (Hill et al. 2000). Smaller cations, such as the HFSE and Lu, can enter the M1 site, and are consequently strongly correlated with $X^{iv}Al$, indicating a coupled substitution: If an Al^{3+} substitutes for Si^{4+} on the tetrahedral site, this will create a charge deficiency, which might be compensated by a charge transfer to the M1 site (Hill et al. 2000).

The correlation between D_{Lu} as an HREE with $X^{IV}Al$ (Supplementary Figure S7) is a strong indicator that Lu^{3+} can occupy both the M2 and the M1 site (Fig. 3a). This is especially relevant for clinopyroxene enriched in Fe^{3+} but the proportion of HREE on the M1 decreases with increasing $X^{IViv}Al$ and Mg^{2+} (Baudouin et al. 2020) and hence the effect in our data is not very pronounced. Contrasting 3+ ions, the substitution of 2+ ions into the clinopyroxene lattice does not require charge balance. This is underlined by the fact that e.g., the $X^{IV}Al$ in clinopyroxene does not correlate with D_{Sr} (Supplementary Figure S7).

The correlation of D_{HFSE} with Fe and between Fe and Ti on the M1 side of clinopyroxene suggests that the compatibility of REE and HFSE increases with an increasing hedenbergite component in clinopyroxene (Dygert et al. 2014). In lunar clinopyroxene, where Fe is present only as Fe^{2+}, Fe^{2+} and Mg^{2+} compete for the same site (Supplementary Figure S7). $D^{cpx-melt}$ of light REE (La, Sm, Nd), however, are negatively correlated with Fe (Supplementary Figure S7). The hedenbergite component in clinopyroxene increases the compatibility of HREE and HFSE, but seems to decrease the compatibility of larger REE ions entering the M2 site.

In the compiled clinopyroxene data ^{iv}Al and D_{Ti} are only weakly correlated ($R^2 = 0.4$; Supplementary Figure S7, Fig. 4c), which seems in contradiction with literature (e.g., Hill et al. 2000). This could be a consequence of the fact, that Ti in our experimental runs is not a trace element but a minor element (0.5–1.5 wt% TiO_2). The correlation matrix implies a strong linear correlation between Q_{TiSi} ($Q_{TiSi} = [TiO_2^{mineral} * SiO_2^{melt}]/[TiO_2^{melt} * SiO_2^{mineral}]$) and $D^{cpx-melt}$ of the HFSE Supplementary Figure S7 and Fig. 4). In high-Ti melts (e.g., CHV-6B and high Ti compositions in Leitzke et al. 2016), $D^{cpx-melt}$ for Hf and Lu are comparatively low (Fig. 4a, b). We suggest that a relatively high abundance of TiO_2 in a melt decreases the activity of HFSE in the melt and this will decrease D_{HFSE} because less HFSE will partition into the coexisting minerals. Similarly, if TiO_2 in the clinopyroxene is relatively high, compared to the melt. D_{HFSE} will be high, since the HFSE will "follow" the Ti. This behavior is expressed by the newly defined Q_{TiSi} (Fig. 4). Data for experiments on composition CHV-6B and for high-Ti melts and clinopyroxene in Leitzke et al. (2016) suggest that clinopyroxene accommodates a maximum of about 2–3.5 wt% TiO_2, whereas a coexisting melt can contain up to 12 wt% of TiO_2 without crystallizing any other Ti-containing mineral phase (Leitzke et al. 2016). We infer that until saturation of clinopyroxene in terms of Ti is reached, $D^{mineral-melt}$ for all similarly behaving ions, like D_{Hf} and D_{Lu} will be elevated, as suggested by Mysen et al. (1980) and we conclude that the highest $D^{cpx-melt}$ for HFSE are found in bulk compositions with 2–4 wt% TiO_2 (composition CHV-6C, and Dygert et al. 2014). It is interesting to note that at ~ 3.5 mol% TiO_2 (corresponding to 4.4 wt%) the silicate melt network begins to depolymerize, which will also influence the capability of the melt structure to incorporate Ti and HFSE (Mysen and Neuville 1995).

Overall, our new data underline the effect of $X^{IV}Al$ on $D^{cpx-melt}$ (Dygert et al. 2014), where small radius ions compensate for the charge balance and partition preferentially into M1. Nevertheless, the predictive models for trace element partition coefficients based on ^{iv}Al fail to predict our data (Supplementary Figures S3, S4). Similarities between our clinopyroxene dataset and Dygert et al. (2014) indicate that temperature, Fe content, and $X^{IV}Al$ in clinopyroxene are the most important factors controlling $D^{cpx-melt}$ but predictive models do not yet account for all these parameters. Titanium distribution between silicate and melt seems to be an additional factor that should be considered in order to describe and predict the partitioning behavior of HFSE (cf. Mysen et al. 1980, 1995).

Pigeonite and orthopyroxene (low-Ca pyroxenes)

In contrast to Dygert et al. (2020) and Sun and Liang (2013), we see a pronounced negative D_{Eu} anomaly in all experiments with low-Ca pyroxenes at reducing conditions, which is caused by the incorporation of Eu^{2+} into pyroxene. Lattice strain parameters for our $D^{pigeonite-melt}$ diverge from the data of Dygert et al. (2020) (Supplementary Table S5) as D_0 is very sensitive to the major element composition ($X_{WoEnFs} = 9.5–10.5$, 75–78, and 12.4–15 in our data vs. 11,

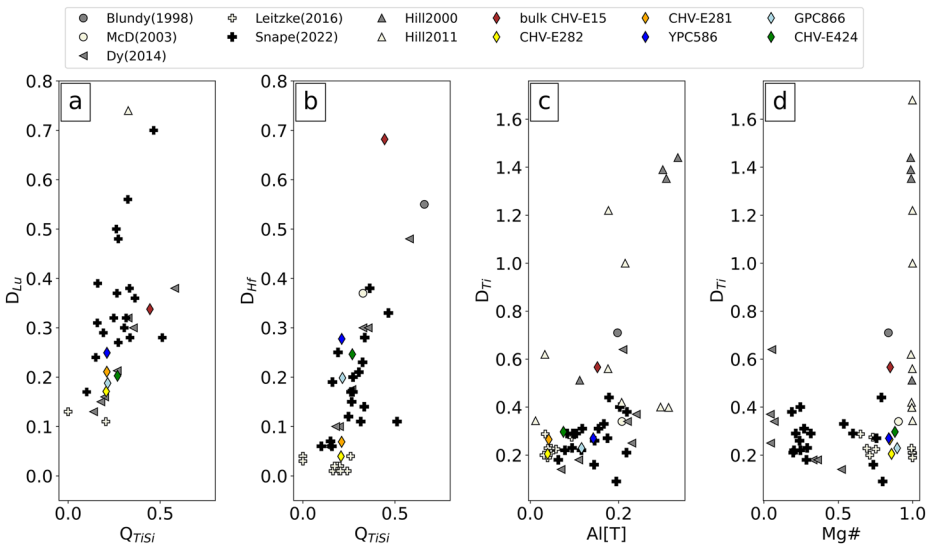

Fig. 4 Correlation between(Q_{TiSi} and $D^{cpx-melt}$ (**a**: Lu, **b**: Hf) and between Ti $D^{cpx-melt}$ and $X^{iv}A$ (**c**) and Mg# (**d**). Data from Dygert et al. (2014) (left pointed triangles: Dy2014), Snape et al. (2022) (black crosses: Snape2022), Leitzke et al. (2016) (white crosses: Leitzke2016), Hill et al. (2000, 2011) (grey and white triangles: Hill et al. 2000, 2011), Blundy et al. (1998) (grey circle: Blundy1998), McDade et al. (2003) (beige circle: McD2003). Diamond depicts values of this study as in Fig. 2

65, 24 for Eu14-17 in Dygert et al. 2020) and temperature. At lower temperatures and fO_2 (1125 °C and FMQ, Dygert et al. 2020), D_{REE} are less incompatible in pigeonite. The difference within our pigeonite data could be a result of pigeonite chemistry in CHV-E281 and 282 ($Wo_{10-9}En_{75-78}Fs_{15-12}$). The E of CHV-E281 pigeonite (E = 327.8 GPa) is similar to E of orthopyroxene of Sun and Liang (2013) (E = 193–295 GPa). Due to the broad mismatch of our pigeonite and orthopyroxene fitting parameters with the data of Sun and Liang (2013), it is not surprising that their parameterized model fails to predict the partition coefficients of our study (cf. Supplementary Figure S5 for HFSE).

Plagioclase

The comparison of our data with the data of Aigner-Torres et al. (2007) shows, that D_{REE} between plagioclase and melt depend on fO_2 (experiment 36 of Aigner-Torres et al. was performed at ΔIW + 11.5 and 35 at IW) and potentially also on the anorthite component in plagioclase (molar fraction of anorthite: 74–77 in Aigner-Torres et al. 2007, instead of 94–99 in this study and Dygert et al. 2020) as discussed by e.g., Blundy and Wood (1991) and Sun et al. (2017). Partition coefficients of trace elements between plagioclase and melt increase with fO_2 being more oxidizing. Our lattice strain fit parameters for the divalent ions (Supplementary Figure S6; Supplementary Table S5) agree well with data from Dygert et al. (2020) and Sun and Liang (2017). Comparing our data with Dygert et al. (2020), we find that the temperature effect on partition coefficients is minor (1200 °C in our experiments and 1100 °C in Dygert et al. 2020).

Olivine

We present a large dataset for olivine-melt trace element partition coefficients at reducing conditions, which will be essential for modeling trace element evolution in a magma ocean, such as on the Moon. The lattice strain model fits show that D_0 for 3+ ions (D_{REE} + Sc) increase with decreasing temperature (D_0 = 0.06 and 0.19–0.27, Supplementary Table S5). Scandium and the light REE are more compatible in olivine that crystallized at 1200 °C (CHV-E281/82), than at 1270 °C (CHV-E421). The Li partition coefficient is one magnitude higher in low-T olivine, compared to high-T olivine (D_{Li} = 0.3 vs. 0.03). Natural lunar olivine data from Chen et al. (2022) for olivine-melt inclusion partitioning are similar to our low-T partition coefficients. D_{Li} does not depend on olivine Mg# in our experiments (forsterite proportions of 0.84–0.85 in all experimental olivine), as was proposed by Chen et al. (2022). The D_V and D_{Cr} at 1200 °C are about half a magnitude higher, than data for olivine crystallized at 1270 °C (0.9 and 1.04 to 0.12 and 0.25, respectively), which will significantly influence the trace element compositions of the melts from which olivine crystallizes during almost the entire crystallization sequence of the LMO (Schmidt and Kraettli 2022).

Application of $D^{mineral-melt}$ to lunar magma ocean modeling

Given the aforementioned effects of T, P, and fO_2, choosing the appropriate trace element $D^{mineral-melt}$ is extremely important for modeling the trace element and isotopic evolution in the cooling LMO. Here, we investigate how our new set of $D^{mineral-melt}$ affects the trace element composition of a crystallizing LMO.

Bulk silicate Moon compositions and experimental solidification sequences

Several previous studies investigated the crystallization sequence of the LMO by either applying thermodynamic modeling (Snyder et al. 1992; Elkins-Tanton et al. 2011; Johnson et al. 2021) or high-pressure high-temperature experiments (Elardo et al. 2011; Lin et al. 2017; Charlier et al. 2018; Rapp and Draper 2018; Schmidt and Kraettli 2022; Jing et al. 2022). We use two of the most recent experimental studies that used endmember lunar mantle compositions (i.e., Rapp and Draper (2018): "Lunar Primitive Upper Mantle" of J. Longhi (LPUM) and Schmidt and Kraettli (2022): Taylor Whole Moon (TWM)). The chemical differences of these two bulk compositions of the LMO affects the sequence of minerals crystallizing from the LMO with falling temperatures. This becomes especially important when the LMO has undergone significant crystallization (i.e., > 70 vol percent crystallized solid"-PCS). The differences are further visualized in Fig. 5a, b. Both studies assume that the lunar mantle was completely molten with an initial depth of the LMO of ~ 1200 km.

Both crystallization sequences (Fig. 5a, b) crystallize olivine first, followed by varying amounts of orthopyroxene. In sequence 1 at about 70 PCS, the mineralogy of the precipitate is dominated by plagioclase and clinopyroxene and minor amounts of olivine and spinel (Fig. 5a). Clinopyroxene dominates until ~ 90 PCS and plagioclase and pigeonite dominate until 99.5 PCS. In the last fractionation step, pigeonite is replaced by clinopyroxene and crystallizes with plagioclase and traces of olivine, pigeonite, ilmenite, quartz, together with 2 vol% of apatite. In the Schmidt and Kraettli (2022) crystallization sequence (sequence 2; Fig. 5b) Cr-spinel is the first phase after olivine and orthopyroxene, appearing at ~ 53 PCS. Clinopyroxene appears after 69 PCS, and no pigeonite is present. Plagioclase crystallizes after 74 PCS, followed by Ti-rich spinel (ulvöspinel-ulv) after 93

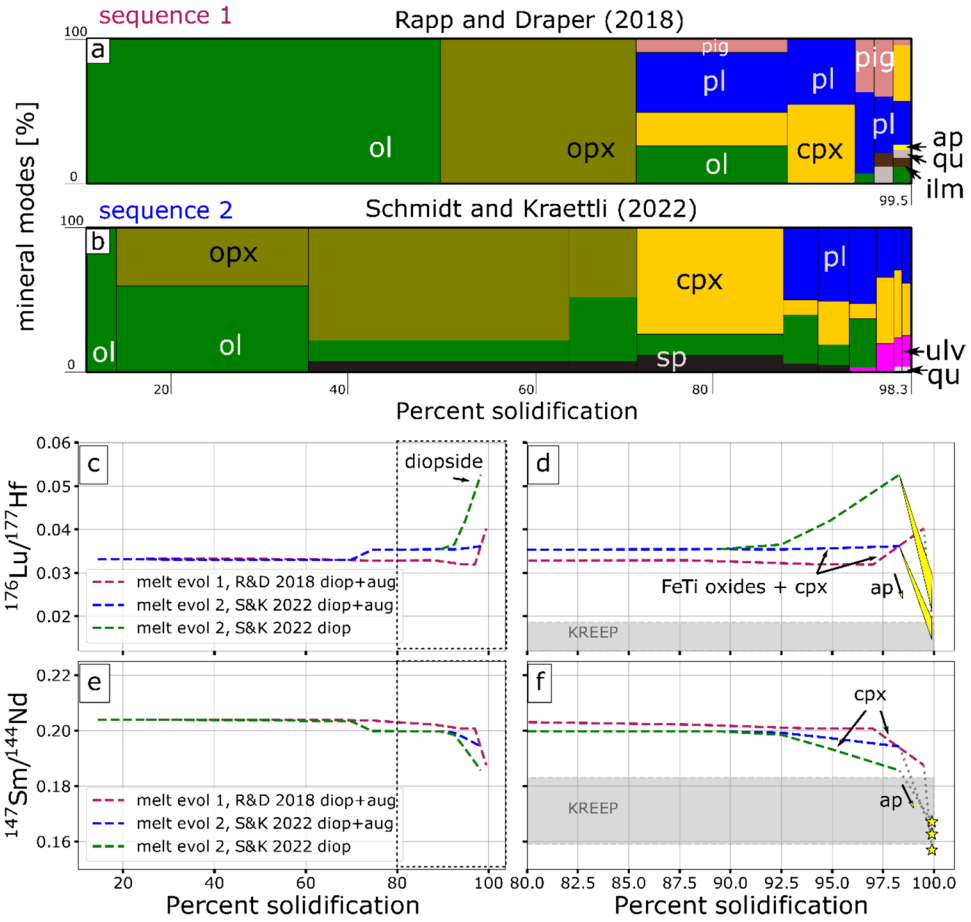

Fig. 5 Mineral precipitates (cumulates with modal mineralogy in vol%) from the LMO based on experimentally determined sequences of different bulk silicate Moon compositions and isotopic evolution of the remaining melt upon cumulate fractionation from the LMO. **a** LPUM (Longhi 2003, 2006) conducted by Rapp and Draper (2018) and **b** TWM (Taylor 1982) by Schmidt and Kraettli (2022). Both crystallization sequences **a**, **b** show that olivine (ol) crystallizes first, followed by different amounts of orthopyroxene (opx). Sequence 2 crystallizes very small amounts of spinel (sp). At about 70% crystallization (percent cystallized solid, PCS) variable amounts of plagioclase (pl) and clinopyroxene (cpx) and/or pigeonite (pig) begin to precipitate. Sequence 1 (Rapp and Draper, **a**) crystallizes additional traces of ilmenite (ilm), quartz (qu), and apatite after 97 PCS, whereas sequence 2 (Schmidt and Kraettli, **b**) crystallizes clinopyroxene, plagioclase, minor amounts of fayalite, and finally ulvöspinel (ulv) from 90 PCS onwards, together with very small modal amounts of quartz (qu). Note that none of the sequences reaches 100 PCS. Color coding as follows: green = olivine; olive green = orthopyroxene; yellow = clinopyroxene; blue = plagioclase; pink = Fe-Ti oxides; rose-pigeonite; bright yellow = apatite; black = spinel; brown = ilmenite; grey = quartz. **c**–**f** calculated isotopic evolution of $^{176}Lu/^{177}Hf$ (Fig. 5c + d) and $^{147}Sm/^{144}Nd$ (Fig. 5 e + f) of the residual liquid of the LMO based crystallization sequences (**a**, **b**) covering 15–100 percent solidification (**c**, **e**) and 80–100 percent solidification (**d**, **f**). Details of the calculations are given in the text and in the supplementary material (Methods and Table S6). The brown evolution line (R&D2018) corresponds to sequence 1; calculations were performed using diopside and augite (diop + aug). Two evolution lines after Schmidt and Kraettli (2022) for $^{176}Lu/^{177}Hf$ and $^{147}Sm/^{144}Nd$ with either purely diopside (green lines) or diopside and augite (blue lines). Note the isotopic signature of urKREEP (d + f grey shaded area) reservoir is inferred from natural samples (Borg et al. 2009, 2020; Gaffney and Borg 2014; Edmunson et al. 2009) (**d**) yellow triangles give the trend in $^{176}Lu/^{177}Hf$ if significant amounts of additional apatite (20–30 vol%) and plagioclase (80–70 vol%) crystallize (**d**). The spread in $^{147}Sm/^{144}Nd$ is minor, only the scenario with 23% ap + 77% pl is shown. See text for details

PCS. No ilmenite occurs, neither does apatite. Only traces of quartz appear in the last percent of the crystallizing LMO (Schmidt and Kraettli 2022).

Modeling the isotopic evolution during the cooling of the lunar magma ocean

To model the trace element evolution of the solidifying LMO, we assume that the initial trace element composition of the LMO was chondritic (e.g., Rapp and Draper 2018; using CI of McDonough and Sun 1995). We use a model that

considers equilibrium fractionation until < 50 PCS, followed by fractional crystallization until full solidification (Snyder et al. 1992; Supplementary Material Methods). We tested if full fractional crystallization over the entire LMO crystallization affects the outcome and found that this has only negligible effects on the investigated ratios. Furthermore, we use our new partition coefficients for silicates and literature data for accessory phases (details are listed in the Supplementary material and Supplementary Table S6) and the crystallization sequences of Rapp and Draper (2018) and Schmidt and Kraettli (2022) (Fig. 5a, b) to calculate Sm/Nd and Lu/Hf. We further calculated all trace element abundances in the evolving LMO along a fractionation sequence of Schmidt and Kraettli (2022) for elements with reliable trace element partition coefficients, determined in this study (Li, Ba, Th, U, Sc, Ti, V, Cr, Mn, Co, Ni, Nb, Ta, La, Ce, Pr, Nd, Sm, Zr, Hf, Eu, Gd, Tb, Dy, Y, Ho, Er, Tm, Yb, Lu).

The calculated elemental Sm/Nd and Lu/Hf of the evolving melts were transformed to isotopic ratios $^{147}Sm/^{144}Nd$ and $^{176}Lu/^{177}Hf$ by correcting with the chondritic isotopic abundances ($^{147}Sm/^{144}Nd = 0.196$, $^{176}Lu/^{177}Hf = 0.0336$; Bouvier et al. 2008). We noted, that the use of partition coefficients for either diopside or augite has no strong influence on $^{147}Sm/^{144}Nd$ because partition coefficients are very similar (Fig. 2a and Supplementary Table S6). However, the coefficients for Lu and Hf between diopside and augite are significantly different ($D_{Lu}/D_{Hf} = 0.34/0.68$ and 0.17/0.04, diopside and augite, respectively). We show the evolution lines for either diopside (green line) or diopside and augite (blue line) in Fig. 5c–f. We used both diopside or augite partition coefficients, as clinopyroxenes evolve towards less calcic endmembers during LMO solidification (cf. Supplementary Figure S1). Details about the partition coefficients can be found in the Supplementary Table S6. Figure 6 shows the calculated absolute trace element abundances during the fractionation of the LMO. The results are compared to the absolute trace element contents of urKREEP as modeled by Warren and Wasson (1979).

Evolution of $^{176}Lu/^{177}Hf$ and $^{147}Sm/^{144}Nd$

Our trace element modeling for $^{176}Lu/^{177}Hf$ (Fig. 5c–f) shows that the evolution of the ratios of the two fractionation sequences are virtually identical until ~ 90 PCS, which corresponds roughly to the onset of the crystallization of lunar high-Ti and Fe cumulates ("Ilmenite-bearing cumulates", Snyder et al. 1992). The crystallization of clinopyroxene begins at about 70 PCS and causes a very small increase of $^{176}Lu/^{177}Hf$ (Fig. 5c, d), and a slight decrease of $^{147}Sm/^{144}Nd$ (Fig. 5e, f).

The precipitation of Fe-Ti oxides, which occurs together with clinopyroxene in the last stages of LMO crystallization, causes an increase of $^{176}Lu/^{177}Hf$ to values > 0.4 (Fig. 5c, d), whereas $^{147}Sm/^{144}Nd$ decreases mainly due to clinopyroxene crystallization (Fig. 5e, f). Thereby, it has a strong influence, whether partitioning data for high-Ca diopside, or augite are chosen (green and blue lines, Fig. 5c, d). Neither of the models yield $^{176}Lu/^{177}Hf$ close to the proposed urKREEP isotopic signatures, which were calculated based on lunar samples (Borg et al. 2009, 2020; Gaffney and Borg 2014; Edmunson et al. 2009). This urKREEP is thought to represent the last remaining liquids of the LMO (Warren and Wasson 1979). However, as the KREEP component is known to be rich in phosphorous (P stands for phosphorous), we propose that fractionation of plagioclase together with variable amounts of apatite from the last dregs of LMO melts is needed to attain the correct isotopic signature. According to our model, abundant apatite fractionation (20–30 vol%; Fig. 5d, f) induces a significant fractionation of $^{176}Lu/^{177}Hf$ and only a minor fractionation of $^{147}Sm/^{144}Nd$ in the residual melt (Fig. 5d, f), rendering the remaining liquid fraction closer to the compositions proposed for the urKREEP reservoir. The quantity of plagioclase and apatite may vary due to variations in clinopyroxene and plagioclase partition coefficients (Fig. 5d). The yellow areas in Fig. 5d correspond to the liquid evolution after the removal of a plagioclase-apatite cumulates with 20–30 vol% apatite.

We suggest that phosphates play a yet underestimated role in the trace element evolution of urKREEP. Apatite and whitlockite are abundant accessory phases in lunar rocks (Papike et al. 1991; Elardo et al. 2014; Hu et al. 2021) and indeed apatite has been reported to crystallize towards the final stages of the experimentally determined fractionation sequences (e.g., Rapp and Draper 2018). Note that it could also be whitlockite that crystallizes during late stages of the LMO solidification but as there are no $D^{whitlockite-melt}$, we decided to use $D^{ap-melt}$ for F-apatite (cf. Prowatke and Klemme 2006b; Ji and Dygert 2023).

Phosphate crystallization induces a significant fractionation of $^{176}Lu/^{177}Hf$ and a minor fractionation of $^{147}Sm/^{144}Nd$ in the residual melt (Fig. 5d, f), which dregs the isotopic signatures of the modeled frationation residuum closer to the signatures proposed for the urKREEP reservoir, based on sample evidence (Edmunson et al. 2009; Borg et al. 2009, 2020). This would indicate, however, that the analyzed KREEP-rich natural samples contain traces of the LMO, which formed after 99 PCS and require fractionation of cumulates rich in plagioclase and accessories (e.g., diorite). Our data implies that the urKREEP composition is reached relatively late in the crystallization of the LMO at ~ 99.9 PCS, which is later than suggested previously (e.g., Rapp and Draper 2018; Maurice et al. 2020).

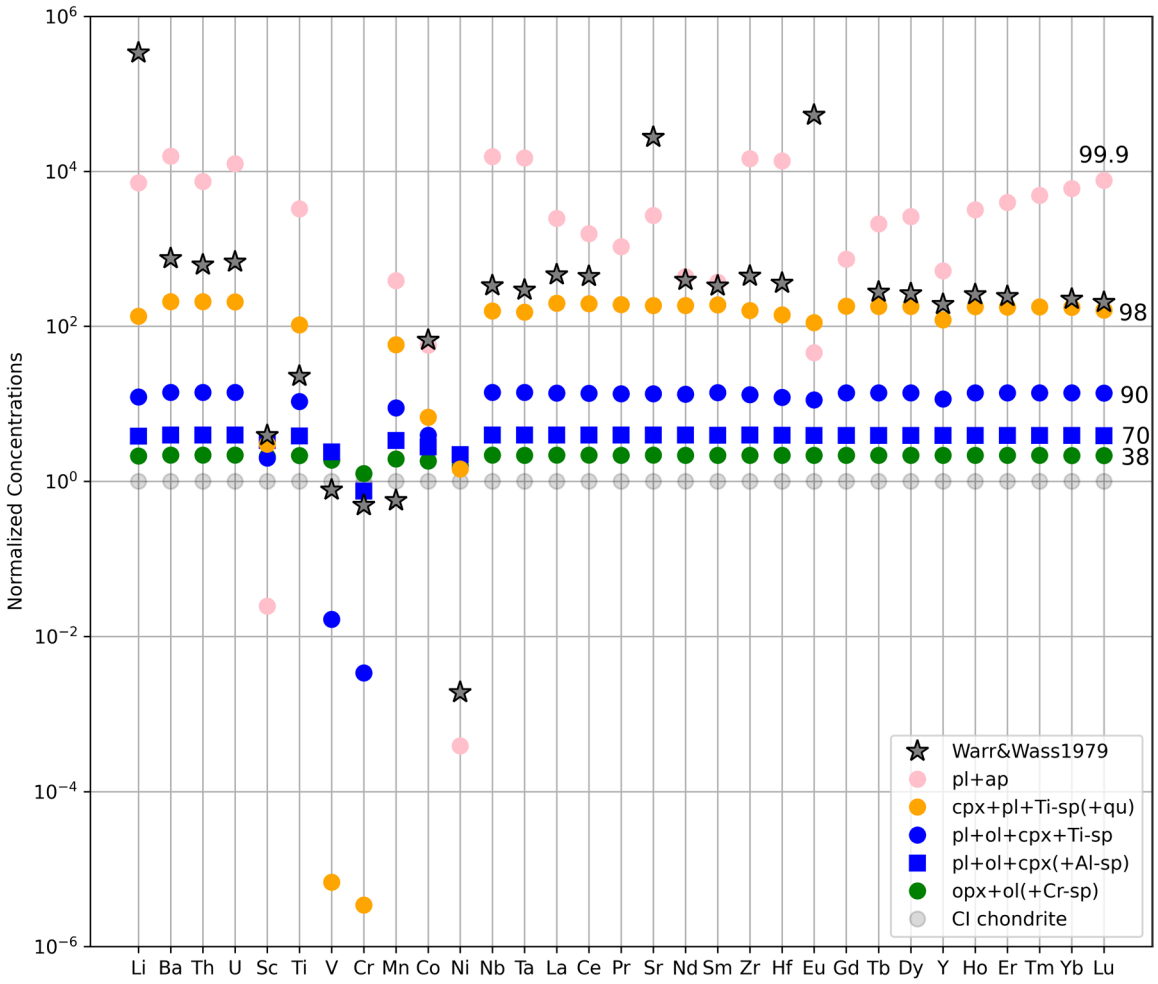

Fig. 6 Calculated trace element compositions (normalized to CI-chondrite of McDonough and Sun 1995) of LMO residuum with progressive crystallization, following Schmidt and Kraettli (2022). With increasing crystallization, trace element concentrations of incompatible elements increase in the remaining melts, whilst the concentrations of compatible elements (e.g., Cr, V, Ni) decrease. Colors correspond to the cumulates which are crystallizing. The numbers on the right side indicate PCS. For comparison, the grey stars correspond to the proposed urKREEP composition as modeled by Warren and Wasson (1979). The lowest concentrations of V and Cr are not shown, due to scaling reasons (cf. Supplementary Table S7)

Modeling the trace element composition of urKREEP

To illustrate the significance of the experimental data, we calculated the abundances of trace elements in the residual liquids during progressive crystal fractionation of the LMO, aiming to constrain the composition of the urKREEP reservoir, as introduced by Warren and Wasson (1979) (Fig. 6, Supplementary Table S7).

The trace element modeling as shown in Fig. 6 visualizes that most elements in the remaining melt (e.g., Ba, Th, U, Zr, REE) develop towards the urKREEP concentrations proposed by Warren and Wasson (1979) up to 98 PCS. Note, that we did not include trapped liquids in our model. Therefore, our modeled trace element concentrations at 98 PCS should be taken as a minimum concentration of these elements in urKREEP. The pink dots in Fig. 6 correspond to the liquid composition after removing a cumulate of plagioclase and apatite, as suggested in this study based on isotopic ratios (Fig. 5). For a few elements (Li, Co, Sm, Nd, and Sr) the fractionation of plagioclase and apatite causes an evolution of the absolute concentrations into the direction of the urKREEP as modeled by Warren and Wasson (1979). Our data suggests that Warren and Wasson (1979) overestimated V and Cr concentrations in urKREEP, but we would like to stress that V and Cr are heavily depleted by plagioclase and apatite fractionation. As we have shown in the discussion on olivine, V and Cr are also compatible in low-T olivine, which further decreases the abundances of these elements in the remaining liquid. Our modeling results highlight, that there is a need for new LMO fractionation models that focus on the late evolution of the LMO, and the composition of urKREEP.

Conclusions and implications

- We determined new trace element partition coefficients ($D^{mineral-melt}$) between clinopyroxene (diopside and augite), pigeonite, orthopyroxene, olivine, plagioclase, and LMO melts for a total of 39 trace elements, including the REE and heat producing elements (K, U, Th). Clinopyroxene $D^{mineral-melt}$ vary with pressure, temperature, and pyroxene chemistry. Low-Ca pyroxene $D^{mineral-melt}$ show similar $D^{mineral-melt}$ for mono- and divalent trace elements. Trivalent ions are generally one magnitude less compatible in low-Ca pyroxene compared to high-Ca pyroxene. $D^{plagioclase-melt}$ agree with literature data (Dygert et al. 2020). The trace element partition coefficients of pigeonite, plagioclase, and olivine extend the existing experimental datasets for Li, Ba, and HFSEs (Zr, Th, U, Nb, Ta) at conditions relevant for the Moon.
- We used our new partition coefficients in conjunction with experimental data on the crystallization of the lunar magma ocean to constrain the trace element evolution of the LMO. Our model indicates that crystallization of additional apatite (or other Ca-rich phosphates) is needed to explain the observed $^{176}Lu/^{177}Hf$ and $^{147}Sm/^{144}Nd$ trace element signature of the KREEP reservoir on the Moon. These findings underline the need to better understand the final stage of LMO crystallization and the need for enhanced models to constrain the temporal evolution of the LMO.
- We modeled an urKREEP trace element composition based on trace element partition coefficients and an experimentally determined LMO crystallization sequence. Our data clearly show that the very last stages of LMO crystallization exert a strong effect on the trace element composition of the final dregs of melts, and consequently urKREEP

Supplementary Information The online version contains supplementary material available at https://doi.org/10.1007/s00410-024-02118-z.

Acknowledgements Data processing was done with the help of python numpy, pandas and seaborn libraries. Figures were drawn with matplotlib and Inkscape free software. We would like to acknowledge the excellent work of the workshops at the Institut für Mineralogie at Universität Münster, especially in regards to the piston-cylinder assemblies and the excellent sample preparation by Maik Trogisch. We would also like to thank Beate Schmitte for her superb help with all things regarding EPMA and LA-ICP-MS. We acknowledge the very helpful comments of the editor O. Müntener, and we thank N. Dygert and an anonymous reviewer for constructive comments and suggestions that helped to significantly improve the paper.

Author contributions Cordula Haupt, Christian Renggli, Arno Rohrbach, Jasper Berndt, Sabrina Schwinger, Maxime Maurice, Doris Breuer, and Stephan Klemme contributed to the conception and design of the project. Funding was acquired by Doris Breuer and Stephan Klemme. Stephan Klemme, Arno Rohrbach, Christian Renggli, Cordula Haupt, and Jasper Berndt developed the experimental and analytical approach. Experiments were run and analyses were performed by Cordula Haupt. Data processing and modeling was done by Cordula Haupt and Maximilian Schulze. The first draft of the manuscript was written by Cordula Haupt. All authors commented on further versions and approved to the final version of the manuscript.

Funding Open Access funding enabled and organized by Projekt DEAL. This research is supported by the Deutsche Forschungsgemeinschaft (DFG) project 263649064 – SFB TRR170, publication no. 211.

Data availability Additional data are available in the electronic supplementary files.

Declarations

Conflict of interest None.

References

Aigner-Torres M, Blundy J, Ulmer P, Pettke T (2007) Laser ablation ICPMS study of trace element partitioning between plagioclase and basaltic melts: an experimental approach. Contrib Mineral Petrol 153:647–667. https://doi.org/10.1007/s00410-006-0168-2

Armstrong JT (1991) Quantitative elemental analysis of individual microparticles with electron beam instruments. In: Heinrich KFJ, Newbury DE (eds) Electron probe quantitation. Springer, pp 261–315

Baudouin C, France L, Boulanger M, Dalou C, Devidal JL (2020) Trace element partitioning between clinopyroxene and alkaline magmas: parametrization and role of M1 site on HREE enrichment in clinopyroxenes. Contrib Mineral Petrol 175:1–15

Bédard JH (2010) Parameterization of the Fe=Mg exchange coefficient (Kd) between clinopyroxene and silicate melts. Chem Geol 274:169–176. https://doi.org/10.1016/j.chemgeo.2010.04.003

Blundy JD, Wood BJ (1991) Crystal-chemical controls on the partitioning of Sr and Ba between plagioclase feldspar, silicate melts, and hydrothermal solutions. Geochim Cosmochim Acta 55:193–209

Blundy JD, Wood BJ (1994) Energetics of element partitioning between minerals and melts. Mineral Mag 58A:101–102. https://doi.org/10.1180/minmag.1994.58A.1.56

Blundy JD, Robinson JAC, Wood BJ (1998) Heavy REE are compatible in clinopyroxene on the spinel lherzolite solidus. Earth Planet Sci Lett 160:493–504. https://doi.org/10.1016/S0012-821X(98)00106-X

Borg LE, Gaffney AM, Shearer CK et al (2009) Mechanisms for incompatible-element enrichment on the Moon deduced from the lunar basaltic meteorite Northwest Africa 032. Geochim Cosmochim Acta 73:3963–3980. https://doi.org/10.1016/j.gca.2009.03.039

Borg LE, Connelly JN, Boyet M et al (2011) Chronological evidence that the Moon is either young or did not have a global magma ocean. Nature 477(7362):70–72. https://doi.org/10.1038/nature10328

Borg LE, Cassata WS, Wimpenny J et al (2020) The formation and evolution of the Moon's crust inferred from the Sm-Nd isotopic systematics of highlands rocks. Geochim Cosmochim Acta 290:312–332. https://doi.org/10.1016/j.gca.2020.09.013

Bose K, Ganguly J (1995) Quartz-coesite transition revisited: Reversed experimental determination at 500–1200 C and retrieved thermochemical properties. Am Mineral 80:231–238

Bouvier A, Vervoort JD, Patchett PJ (2008) The Lu–Hf and Sm–Nd isotopic composition of CHUR: constraints from unequilibrated chondrites and implications for the bulk composition of terrestrial planets. Earth Planet Sci Lett 273:48–57. https://doi.org/10.1016/j.epsl.2008.06.010

Boyd FR, England JL (1960) Apparatus for phase-equilibrium measurements at pressures up to 50 kilobars and temperatures up to 1750°C. J Geophys Res 65:741–748. https://doi.org/10.1029/JZ065i002p00741

Brice JC (1975) Some thermodynamic aspects of the growth of strained crystals. J Cryst Growth 28:249–253. https://doi.org/10.1016/0022-0248(75)90241-9

Canup RM, Righter K (2000) Origin of the Earth and Moon. University of Arizona Press

Charlier B, Grove TL, Namur O, Holtz F (2018) Crystallization of the lunar magma ocean and the primordial mantle-crust differentiation of the Moon. Geochim Cosmochim Acta 234:50–69

Chen S, Ni P, Zhang Y, Gagnon (2022) Trace element partitioning between olivine and melt in lunar basalts. Am Mineral 107:1519–1531

Donaldson CH, Usselman TM, Williams RJ, Lofgren GE (1975) Experimental modeling of the cooling history of Apollo 12 olivine basalts. In: Proceedings of the 6th Lunar Science Conference

Dygert N, Liang Y, Hess P (2013) The importance of melt TiO2 in affecting major and trace element partitioning between Fe–Ti oxides and lunar picritic glass melts. Geochim Cosmochim Acta 18:134–151. https://doi.org/10.1016/j.gca.2012.12.005

Dygert N, Liang Y, Sun C, Hess P (2014) An experimental study of trace element partitioning between augite and Fe-rich basalts. Geochim Cosmochim Acta 132:170–186. https://doi.org/10.1016/j.gca.2014.01.042

Dygert N, Liang Y, Sun C, Hess P (2015) Corrigendum to "An experimental study of trace element partitioning between augite and Fe-rich basalts" [Geochim Cosmochim Ac 132 (2014) 170–186]. Geochim Cosmochim Acta 149:281–283

Dygert N, Draper DS, Rapp JF et al (2020) Experimental determinations of trace element partitioning between plagioclase, pigeonite, olivine, and lunar basaltic melts and an fO2 dependent model for plagioclase-melt Eu partitioning. Geochim Cosmochim Acta 279:258–280. https://doi.org/10.1016/j.gca.2020.03.037

Edmunson J, Borg LE, Nyquist LE, Asmerom Y (2009) A combined Sm–Nd, Rb–Sr, and U–Pb isotopic study of Mg-suite norite 78238: further evidence for early differentiation of the Moon. Geochim Cosmochim Acta 73:514–527. https://doi.org/10.1016/j.gca.2008.10.021

Elardo SM, Draper DS, Shearer CK (2011) Lunar Magma Ocean crystallization revisited: bulk composition early cumulate mineralogy and the source regions of the highlands Mg-suite. Geochim Cosmochim Acta 75:3024–3045. https://doi.org/10.1016/j.gca.2011.02.033

Elardo SM, Shearer CK, Fagan AL et al (2014) The origin of young mare basalts inferred from lunar meteorites Northwest Africa 4734, 032, and LaPaz Icefield 02205. Meteorit Planet Sci 49:261–291. https://doi.org/10.1111/maps.12239

Elkins-Tanton LT, Burgess S, Yin Q-Z (2011) The lunar magma ocean: reconciling the solidification process with lunar petrology and geochronology. Earth Planet Sci Lett 304:326–336. https://doi.org/10.1016/j.epsl.2011.02.004

Gaffney AM, Borg LE (2014) A young solidification age for the lunar magma ocean. Geochim Cosmochim Acta 140:227–240. https://doi.org/10.1016/j.gca.2014.05.028

Goldschmidt VM (1937) The principles of distribution of chemical elements in minerals and rocks. The seventh Hugo Müller Lecture, delivered before the Chemical Society on March 17th, 1937. J Chem Soc. https://doi.org/10.1039/JR9370000655

Grove TL (1982) Use of FePt alloys to eliminate the iron loss problem in 1 atmosphere gas mixing experiments: theoretical and practical considerations. Contrib Mineral Petrol 78:298–304. https://doi.org/10.1007/BF00398924

Haupt CP, Renggli CJ, Klaver M et al (2023) Experimental and petrological investigations into the origin of the lunar Chang'e 5 basalts. Icarus. https://doi.org/10.1016/j.icarus.2023.115625

Hauri EH, Wagner TP, Grove TL (1994) Experimental and natural partitioning of Th, U, Pb and other trace elements between garnet, clinopyroxene and basaltic melts. Chem Geol 117:149–166

Herzenberg CL, Riley DL (1970) Mössbauer spectrometry of lunar samples. Science 167:683–686. https://doi.org/10.1126/science.167.3918.683

Hill E, Wood BJ, Blundy JD (2000) The effect of Ca-Tschermaks component on trace element partitioning between clinopyroxene and silicate melt. Lithos 53:203–215. https://doi.org/10.1016/S0024-4937(00)00025-6

Hill E, Blundy JD, Wood BJ (2011) Clinopyroxene–melt trace element partitioning and the development of a predictive model for HFSE and Sc. Contrib Mineral Petrol 161:423–438. https://doi.org/10.1007/s00410-010-0540-0

Hu S, He H, Ji J et al (2021) A dry lunar mantle reservoir for young mare basalts of Chang'E-5. Nature 600:49–53

Jackson SE (2001) The application of Nd: YAG lasers in LA-ICP-MS. In: Laser-ablation-ICPMS in the Earth sciences: principles and applications. Mineralogical Association of Canada, pp 29–45

Ji D, Dygert N (2023) Trace element partitioning between apatite and silicate melts: effects of major element composition, temperature, and oxygen fugacity, and implications for the volatile element budget of the lunar magma ocean. Geochim Cosmochim Acta 369:141–159

Jing J-J, Lin Y, Knibbe JS, van Westrenen W (2022) Garnet stability in the deep lunar mantle: constraints on the physics and chemistry of the interior of the Moon. Earth Planet Sci Lett 584:117491. https://doi.org/10.1016/j.epsl.2022.117491

Jochum KP, Weis U, Stoll B et al (2011) Determination of reference values for NIST SRM 610–617 Glasses Following ISO guidelines. Geostand Geoanal Res 35:397–429. https://doi.org/10.1111/j.1751-908X.2011.00120.x

Johnson TE, Morrissey LJ, Nemchin AA et al (2021) The phases of the Moon: modelling crystallisation of the lunar magma ocean through equilibrium thermodynamics. Earth Planet Sci Lett 556:116721. https://doi.org/10.1016/j.epsl.2020.116721

Klemme S, O'Neill HSC (1997) The reaction MgCr2O4+ SiO2= Cr2O3+ MgSiO3 and the free energy of formation of magnesiochromite (MgCr2O4). Contrib Mineral Petrol 130:59–65

Klemme S, Günther D, Hametner K et al (2006) The partitioning of trace elements between ilmenite, ulvospinel, armalcolite and silicate melts with implications for the early differentiation of the moon. Chem Geol 234:251–263. https://doi.org/10.1016/j.chemgeo.2006.05.005

Krawczynski MJ, Grove TL (2012) Experimental investigation of the influence of oxygen fugacity on the source depths for high

titanium lunar ultramafic magmas. Geochim Cosmochim Acts 79:1–19. https://doi.org/10.1016/j.gca.2011.10.043
Leitzke FP, Fonseca ROC, Michely LT et al (2016) The effect of titanium on the partitioning behavior of high-field strength elements between silicates, oxides and lunar basaltic melts with applications to the origin of mare basalts. Chem Geol 440:219–238. https://doi.org/10.1016/j.chemgeo.2016.07.011
Lin Y, Tronche EJ, Steenstra ES, van Westrenen W (2017) Experimental constraints on the solidification of a nominally dry lunar magma ocean. Earth Planet Sci Lett 471:104–116. https://doi.org/10.1016/j.epsl.2017.04.045
Longhi J (2003) A new view of lunar ferroan anorthosites: postmagma ocean petrogenesis. J Geophys Res Planets 108:2–16
Longhi J (2006) Petrogenesis of picritic mare magmas: constraints on the extent of early lunar differentiation. Geochim Cosmochim Acta 70:5919–5934. https://doi.org/10.1016/j.gca.2006.09.023
Mallik A, Ejaz T, Shcheka S, Garapic G (2019) A petrologic study on the effect of mantle overturn: implications for evolution of the lunar interior. Geochim Cosmochim Acta 250:238–250. https://doi.org/10.1016/j.gca.2019.02.014
Mallmann G, O'Neill HSC (2009) The crystal/melt partitioning of V during mantle melting as a function of oxygen fugacity compared with some other elements (Al, P, Ca, Sc, Ti, Cr, Fe, Ga, Y, Zr and Nb). J Petrol 50:1765–1794. https://doi.org/10.1093/petrology/egp053
Mallmann G, Burnham AD, Fonseca ROC (2021) Mineral-melt partitioning of redox-sensitive elements. In: Magma redox geochemistry. American Geophysical Union (AGU), pp 345–367
Maurice M, Tosi N, Schwinger S et al (2020) A long-lived magma ocean on a young Moon. Sci Adv 6:eaba8949. https://doi.org/10.1126/sciadv.aba8949
McDade P, Blundy JD, Wood BJ (2003) Trace element partitioning on the Tinaquillo Lherzolite solidus at 1.5 GPa. Phys Earth Planet in 139:129–147. https://doi.org/10.1016/S0031-9201(03)00149-3
McDonough WF, Sun S-S (1995) The composition of the Earth. Chem Geol 120:223–253
Medard E, McCammon CA, Barr JA, Grove TL (2008) Oxygen fugacity, temperature reproducibility, and H2O contents of nominally anhydrous piston-cylinder experiments using graphite capsules. Am Mineral 93:1838–1844. https://doi.org/10.2138/am.2008.2842
Muir AH, Housley RM, Grant RW et al (1970) Mössbauer spectroscopy of Moon samples. Science 167:688–690. https://doi.org/10.1126/science.167.3918.688
Mysen B, Neuville D (1995) Effect of temperature and TiO2 content on the structure of Na2Si2O5–Na2Ti2O5 melts and glasses. Geochim Cosmochim Acta 59:325–342. https://doi.org/10.1016/0016-7037(94)00290-3
Mysen B, Ryerson FJ, Virgo D (1980) The influenceof TiO2 on the structure and derivative properties of silicate melts. Am Mineral 65:1150–1165
O'Neill HSC (1991) The origin of the moon and the early history of the earth—a chemical model. Part 1: the moon. Geochim Cosmochim Ac 55:1135–1157. https://doi.org/10.1016/0016-7037(91)90168-5
Olin PH, Wolff JA (2010) Rare earth and high field strength element partitioning between iron-rich clinopyroxenes and felsic liquids. Contrib Mineral Petrol 160:761–775. https://doi.org/10.1007/s00410-010-0506-2
Onuma N, Higuchi H, Wakita H, Nagasawa H (1968) Trace element partition between two pyroxenes and the host lava. Earth Planet Sci Lett 5:47–51. https://doi.org/10.1016/S0012-821X(68)80010-X
Papike J, Taylor L, Simon S (1991) Lunar minerals. In: Lunar sourcebook: a user's guide to the Moon. Cambridge University Press, Cambridge, pp 121–181
Prowatke S, Klemme S (2006a) Rare earth element partitioning between titanite and silicate melts: Henry's law revisited. Geochim Cosmochim Acta 70:4997–5012. https://doi.org/10.1016/j.gca.2006.07.016
Prowatke S, Klemme S (2006b) Trace element partitioning between apatite and silicate melts. Geochim Cosmochim Acta 70:4513–4527
Putirka KD (2008) Thermometers and barometers for volcanic systems. Rev Mineral Geochem 69:61–120. https://doi.org/10.2138/rmg.2008.69.3
Rapp JF, Draper DS (2018) Fractional crystallization of the lunar magma ocean: updating the dominant paradigm. Meteorit Planet Sci 53:1432–1455. https://doi.org/10.1111/maps.13086
Roeder PL, Emslie RF (1970) Olivine-liquid equilibrium. Contrib Mineral Petrol 29:275–289. https://doi.org/10.1007/BF00371276
Sato M (1976) Oxygen fugacity and other thermochemical parameters of Apollo 17 high-Ti basalts and their implications on the reduction mechanism. In: Proceedings of the 7th lunar and planetary science conference, pp 1323–1344
Schmidt MW, Kraettli G (2022) Experimental crystallization of the lunar magma ocean, initial selenotherm and density stratification, and implications for crust formation, overturn and the bulk silicate moon composition. J Geophys Res Planets 127:e2022JE007187. https://doi.org/10.1029/2022JE007187
Schwinger S, Breuer D (2022) Employing magma ocean crystallization models to constrain structure and composition of the lunar interior. Phys Earth Planet Inter 322:106831. https://doi.org/10.1016/j.pepi.2021.106831
Shannon RD (1976) Revised effective ionic radii and systematic studies of interatomic distances in halides and chalcogenides. Acta Crystallogr Sect A Cryst Phys Diffr Theor Gen Crystallogr 32:751–767
Shepherd K, Namur O, Toplis MJ et al (2022) Trace element partitioning between clinopyroxene, magnetite, ilmenite and ferrobasaltic to dacitic magmas: an experimental study on the role of oxygen fugacity and melt composition. Contrib Mineral Petrol 177:90. https://doi.org/10.1007/s00410-022-01957-y
Snape JF, Curran NM, Whitehouse MJ et al (2018) Ancient volcanism on the Moon: insights from Pb isotopes in the MIL 13317 and Kalahari 009 lunar meteorites. Earth Planet Sc Lett 502:84–95. https://doi.org/10.1016/j.epsl.2018.08.035
Snape JF, Nemchin AA, Johnson T et al (2022) Experimental constraints on the long-lived radiogenic isotope evolution of the Moon. Geochim Cosmochim Acta 326:119–148. https://doi.org/10.1016/j.gca.2022.04.008
Snyder GA, Taylor LA, Neal CR (1992) A chemical model for generating the sources of mare basalts: combined equilibrium and fractional crystallization of the lunar magmasphere. Geochim Cosmochim Acta 56:3809–3823. https://doi.org/10.1016/0016-7037(92)90172-F
Sossi PA, Klemme S, O'Neill HSC et al (2019) Evaporation of moderately volatile elements from silicate melts: experiments and theory. Geochim Cosmochim Acta 260:204–231. https://doi.org/10.1016/j.gca.2019.06.021
Sun C, Liang Y (2012) Distribution of REE between clinopyroxene and basaltic melt along a mantle adiabat: effects of major element composition, water, and temperature. Contrib Mineral Petrol 163:807–823. https://doi.org/10.1007/s00410-011-0700-x
Sun C, Liang Y (2013) Distribution of REE and HFSE between low-Ca pyroxene and lunar picritic melts around multiple saturation points. Geochim Cosmochim Acta 119:340–358. https://doi.org/10.1016/j.gca.2013.05.036

Sun C, Graff M, Liang Y (2017) Trace element partitioning between plagioclase and silicate melt: the importance of temperature and plagioclase composition, with implications for terrestrial and lunar magmatism. Geochim Cosmochim Acta 206:273–295

Taylor SR (1982) Planetary science: A lunar perspective. Lunar and Planetary Institute Houston

Wadhwa M (2008) Redox conditions on small bodies, the Moon and Mars. Rev Mineral Geochem 68:493–510. https://doi.org/10.2138/rmg.2008.68.17

Warren PH, Wasson JT (1979) The origin of KREEP. Rev Geophys 17(1):73–88. https://doi.org/10.1029/RG017i001p00073

Wood BJ, Blundy JD (1997) A predictive model for rare earth element partitioning between clinopyroxene and anhydrous silicate melt. Contrib Mineral Petrol 129:166–181. https://doi.org/10.1007/s004100050330

Zhang Y, Namur O, Charlier B (2023) Experimental study of high-Ti and low-Ti basalts: liquid lines of descent and silicate liquid immiscibility in large igneous provinces. Contrib Mineral Petrol 178:7. https://doi.org/10.1007/s00410-022-01990-x